

1           **Multiscale electrochemical analysis of the corrosion control of bronze in**  
2           **simulated acid rain by horse-chestnut (*Aesculus hippocastanum L.*) extract as**  
3           **green inhibitor**

4  
5           **Simona Varvara<sup>1,\*</sup>, Giada Caniglia<sup>2</sup>, Javier Izquierdo<sup>2,3,\*\*</sup>, Roxana Bostan<sup>1</sup>, Luiza Găină<sup>4</sup>,**  
6           **Otilia Bobis<sup>5</sup>, Ricardo M. Souto<sup>2,3</sup>**

7  
8           <sup>1</sup> *Department of Exact Sciences and Engineering, “1 Decembrie 1918” University of Alba Iulia,*  
9           *15-17 Unirii St., 510009 Alba-Iulia, Romania*

10           <sup>2</sup> *Department of Chemistry, Universidad de La Laguna, P.O. Box 456, E-38200 La Laguna*  
11           *(Tenerife), Spain*

12           <sup>3</sup> *Institute of Materials and Nanotechnology, Universidad de La Laguna, P.O. Box 456, E-38200*  
13           *La Laguna (Tenerife), Spain*

14           <sup>4</sup> *Department of Organic Chemistry, “Babes-Bolyai” University, 11 Arany Janos St., 400028*  
15           *Cluj-Napoca, Romania*

16           <sup>5</sup> *Life Science Institute, Apiculture and Sericiculture Department, University of Agricultural*  
17           *Sciences and Veterinary Medicine, 3-5 Manastur St., 400028 Cluj-Napoca, Romania*

18  
19  
20           **Abstract**

21           Horse-chestnut ethanolic extract was tested as potential corrosion inhibitor of bronze in  
22           simulated acid rain. The extract was analysed by FTIR, GC-MS and HPLC-PDA, and its anti-  
23           corrosion behaviour studied using a multiscale electrochemical approach (polarization curves,  
24           EIS and scanning electrochemical microscopy), along with SEM-EDS. 94% inhibition efficiency  
25           was attained by developing a surface physisorbed film. A novel methodology for kinetic  
26           evaluation of dynamic adsorption of inhibitive species on metal surface is proposed using  
27           SECM, achieving good agreement with results from conventional electrochemical techniques.  
28           Excellent adsorption-desorption kinetic constants ( $k_a = 0.102 \text{ s}^{-1} \text{ mol}^{-1} \text{ L}$ ;  $k_d = 3.33 \times 10^{-5} \text{ s}^{-1}$ ) were  
29           determined.

30  
31           **Keywords:** bronze; EIS; scanning electrochemical microscopy; potentiodynamic polarization;  
32           adsorption isotherms; corrosion inhibition.

## 33 1. Introduction

34 Copper-tin alloys commonly named bronzes are some of the earliest metallic materials  
35 known by mankind and they were used to produce weapons, tools, statues and ornaments [1].  
36 Due to their excellent electrical and thermal conductivities, hardness and corrosion resistance,  
37 bronzes continue to have widespread applications in various industrial fields, such as building  
38 construction, marine, electronics and electricity, as well as for decorative purposes, artworks and  
39 coinage.

40 In humid atmosphere, bronzes tend to spontaneously passivate by the formation of copper  
41 oxides (namely, cuprite and tenorite) layers on their surfaces [2–4]. Once formed, these oxidised  
42 layers often called *patina* are rather stable acting as protective barriers to the metallic surface  
43 under various exposure conditions [5,6]. Nevertheless, in aggressive environments, such as water  
44 containing carbonates, sulphates, chlorides or nitrates, corrosion may restart even under the  
45 patina, leading to a fast degradation of the bronze surface [7–10]. To overcome this destructive  
46 phenomenon, different protection methods have been developed [3,11–13].

47 The use of organic inhibitors to prevent bronze corrosion has been studied extensively  
48 [14–16], since it is simpler and less expensive than other procedures. Typical organic molecules  
49 used for bronzes protection include benzotriazole and its derivatives [17,18], substituted  
50 imidazoles [19–21], triazole [22,23] and thiadiazole derivatives [12,24–26], Schiff bases [27],  
51 and amino acids [28,29]. Despite their excellent anticorrosive properties, many of these organic  
52 inhibitors are rather expensive and some have been proved to be hazardous for aquatic and  
53 animal life.

54 Due to the increasing awareness of human health and environmental protection, the  
55 development of new effective ‘green’ alternatives to the synthetic corrosion inhibitors has  
56 become mandatory. Most of the environmental-friendly corrosion inhibitors reported in recent  
57 years are based on naturally-produced plant extracts because they are biodegradable, cheap,  
58 readily available at large scale, and renewable sources of materials [30]. In addition, plant  
59 extracts are considered a rich source of naturally synthesized chemical compounds that can be  
60 extracted using quite simple and economically feasible procedures. It was found that the  
61 inhibition performance of plant extracts is usually ascribed to the presence of complex  
62 compounds in their composition, including tannins, flavonoids, alkaloids, phenolics, nitrogen  
63 bases, carbohydrates, proteins and amino acids, as well as hydrolysis products. These natural

64 organic compounds contain heteroatoms (*i.e.*, O, S, and N), aromatic rings and conjugated  
65 double bonds, which could act as adsorption centres to the metallic surface [30].

66 Although various plant extracts have been proposed to be efficient green corrosion  
67 inhibitors for copper [31–36] and brass [37–40] in different environments, their inhibition  
68 potential on bronze corrosion has been scarcely investigated. In a recent paper, Benzidia *et al.*  
69 [41] studied the influence of the tannin extract from the green rind of *Aloe Vera* on B66 bronze  
70 corrosion in 3% NaCl. An inhibition efficiency of 89% was achieved using 150 ppm tannin  
71 extract. Channouf *et al.* [42] showed that *Juniperus communis* presents some anticorrosive  
72 properties on Cu10Sn bronze in 0.5 M NaCl solution. The use of the methanolic extract of *Salvia*  
73 *hispanica* (*S. hispanica*) seeds as a green corrosion inhibitor for bronze in a simulated acid rain  
74 solution was reported by Larios-Galvez *et al.* [43]. They found that *Salvia hispanica* extract acts  
75 as an anodic type-inhibitor, presenting a maximum effectiveness of 96% at 400 ppm. Besides  
76 plant extracts, the bee products, namely propolis [44] and honey [45] were also proved as  
77 efficient green inhibitors of bronze corrosion.

78 The present research focuses on the application of the alcoholic extract of horse chestnut  
79 seeds (*Aesculushippocastanum L.*) as a potential non-toxic corrosion inhibitor for bronze in a  
80 weakly acidic solution containing Na<sub>2</sub>SO<sub>4</sub> and NaHCO<sub>3</sub> (pH 5), simulating an acid rain in the  
81 urban environment. *Aesculushippocastanum L.* is a species of flowering plant in the soapberry  
82 and lychee family *Sapindaceae*. It is native to small areas of the mixed forests in the Pindus  
83 Mountains and the Balkans (South East Europe), although nowadays the horse-chestnut trees are  
84 often found in many parks and cities all over the world. Horse chestnut extracts present high  
85 antioxidant properties, as well as antibacterial, antimicrobial, antiviral, and antifungal effects,  
86 therefore acting as environmentally biocompatible phototherapeutics [46]. Previously, the  
87 alcoholic extract of horse chestnut seeds was successfully used as levelling agent in copper  
88 electrowinning from acidic copper sulphate solution [47], and for lead electrodeposition from  
89 Betts-type electrolytes [48]. More recently, the water extract of horse-chestnut fruit was proved  
90 to be rather effective inhibitor of St3 steel corrosion in tap water [49].

91 In this paper, the anticorrosive properties of the ethanolic extract of horse chestnut (HCE)  
92 on bronze corrosion were investigated by electrochemical methods, *i.e.* potentiodynamic  
93 polarization and electrochemical impedance spectroscopy, as well as by scanning  
94 electrochemical microscopy (SCEM) technique. Several factors were studied, such as inhibitor

95 concentration, immersion time and temperature to assess the best conditions for the inhibition  
96 performance of the horse chestnut extract. In addition, the bronze surface was also examined by  
97 scanning electron microscopy coupled to energy dispersive X-ray spectrometry (SEM-EDS) to  
98 obtain morphological and chemical composition information of the metal-inhibitor system,  
99 whereas Fourier-transform infrared spectroscopy (FTIR), gas chromatography-mass  
100 spectrometry (GC-MS), and high performance liquid chromatography (HPLC)analyses were  
101 used to characterize the extract employed as corrosion inhibitor. The multiscale electrochemical  
102 approach herein employed has shown to be very powerful for the characterization of the surface  
103 interactions heterogeneously and dynamically evolving throughout the metal surface, associated  
104 to inhibitor adsorption and deriving adsorption isotherms. The estimation of the quantitative  
105 kinetic and thermodynamic parameters, along with the evaluation of the surface distribution  
106 upon interaction of the inhibitor, effectively provided complementary and consistent data. To our  
107 knowledge, this is the first time that such quantitative information on adsorption phenomena with  
108 metal-inhibitor systems is achieved using SECM.

109  
110

## 111 **2. Experimental**

### 112 *2.1. Inhibitor preparation*

113 Fresh fruits of *Aesculushippocastanum L.* were collected from a park area in Cluj-  
114 Napoca, Romania in September 2016. The exterior wooden shells were removed and the nut-like  
115 seeds (called conkers or horse-chestnuts) were collected. The horse-chestnut seeds were cleaned  
116 using distilled water and stored for three months in a dark and dry environment, at room  
117 temperature. After that, the dried horse-chestnut seeds were crushed in an agate mortar and a  
118 powder-like material was obtained. 10 g of powdered horse-chestnuts were extracted in 100 mL  
119 of absolute ethanol, in a Soxhlet system for 4h. The ethanolic extract of horse-chestnut was  
120 filtered and centrifuged to remove the traces of solid suspension and it was next evaporated  
121 under reduced pressure at 40°C. Finally, a dark brown almost solid residue was collected and  
122 stored at low temperature in a refrigerator. The residual moisture content (8.63%) was  
123 determined before HCE usage.

124

### 125 *2.2. Chemicals and materials*

126 Analytical grade reagents (Merck, Darmstadt, Germany) and ultra-pure water (Millipore,  
127 18 M $\Omega$  cm) were employed to prepare the corrosive blank electrolyte, consisting of an aqueous  
128 solution of 0.2 g L<sup>-1</sup> Na<sub>2</sub>SO<sub>4</sub> and 0.2 g L<sup>-1</sup> NaHCO<sub>3</sub>, acidified to pH 5 by addition of dilute  
129 H<sub>2</sub>SO<sub>4</sub>. Various amounts of horse chestnut extract were dissolved in the blank corrosive  
130 electrolyte in the concentration range of 0.1 g L<sup>-1</sup> to 1 g L<sup>-1</sup> (w/v).

131 The chemical composition of the bronze was as follows (wt. %): Cu-94.03; Sn-3.31; Pb-  
132 0.24; Zn-1.44; Ni-0.25; Fe-0.22 and S-0.51. Prior to each measurement, the bronze surface was  
133 mechanically abraded using successively 800, 1200 and 4000 grit SiC papers, and finished with  
134 0.3  $\mu$ m alumina slurry resulting in a mirror-like surface. The bronze substrate was then  
135 ultrasonically cleaned in ethanol, thoroughly rinsed with water and dried in air.

136 Phenolic acids and flavonoids (3,4-dihydroxybenzoic acid and quercetin, kaempferol,  
137 myricetin-3-rhamnozide, quercetin rhamnolose, quercetin-3-rhamnozide) were purchased from  
138 Karl-Roth (Karlsruhe, Germany), Sigma-Aldrich (St. Louis, USA) and Fluka (Buchs,  
139 Switzerland). Folin Ciocâlteu reagent, aluminium chloride, sodium carbonate were purchased  
140 from Sigma-Aldrich (St. Louis, USA). Analytical grade solvents were used for HPLC and  
141 spectrophotometric determinations. Deionized water (0.067  $\mu$ S cm<sup>-1</sup>) was produced with a  
142 Millipore Milli-Q assembly.

143

### 144 *2.3. Conventional electrochemical measurements*

145 All conventional electrochemical measurements were performed in a three-electrode  
146 configuration cell. A cylindrical bronze specimen with an exposed area of 0.28 cm<sup>2</sup> was used as  
147 working electrode for the conventional electrochemical investigations. A large platinum grid and  
148 a saturated calomel electrode (SCE) were used as auxiliary and reference electrodes,  
149 respectively. The corrosion tests were carried out using 100 mL of the electrolytes, under non-  
150 stirred and naturally aerated conditions.

151 Electrochemical impedance spectroscopy and potentiodynamic polarization  
152 measurements were carried out using a Princeton Applied Research potentiostat model 2273.  
153 Before each electrochemical test, the bronze sample was left unpolarized in the electrolyte for  
154 1-h to attain a stationary open circuit potential value.

155 Electrochemical impedance spectroscopy measurements (EIS) were performed at the  
156 open circuit potential, in the frequency range from 10 kHz to 10 mHz with 5 points per hertz

157 decade and an *ac* voltage amplitude of  $\pm 10$  mV. To assess the time-stability of the HCE  
158 inhibitive properties on bronze, *ac* impedance experiments were performed at different  
159 immersion times up to 36 h. The obtained impedance data were modelled using *ZSimpWin 3.21*  
160 software.

161 Polarization curves were recorded at constant sweep rate of  $10 \text{ mV min}^{-1}$ , in a wide  
162 potential range of  $\pm 200$  mV *vs.* the open circuit potential, starting from the cathodic to the anodic  
163 direction. The sealed electrochemical cell was thermostatted at various temperatures, namely  
164 298, 308, 318 and 328 K.

165

#### 166 *2.4. Scanning Electrochemical Microscopy (SECM)*

167 SECM experiments were conducted using a scanning electrochemical microscope from  
168 Sensolytics GmbH (Bochum, Germany). The SECM probe was a home-made platinum  
169 microelectrode with a platinum disk of  $12.5 \text{ }\mu\text{m}$  diameter. Microelectrodes were fabricated  
170 following well-established procedures [50]. For this process, the components were borosilicate  
171 glass capillaries of dimensions  $1.5 \text{ mm}$  outer diameter and  $0.375 \text{ mm}$  glass wall from Hilgenberg  
172 GmbH (Massfeld, Germany),  $12.5 \text{ }\mu\text{m}$  diameter platinum wire from Goodfellow (Cambridge,  
173 UK), two-component conductive silver epoxy from RS Components (Corby, UK), and  
174 conductive copper wire, assisted with a Beveller heat pipette-puller from Sutter (Novato, CA,  
175 USA). The fabrication routine and the heat-pulling of the capillaries were optimized to produce  
176 microelectrodes with a cone-shape end. All SECM measurements were done with  
177 microelectrodes presenting an RG ratio (*i.e.*, ratio between the diameters of the Pt micro disk and  
178 the surrounding glass) equal to 40.

179 The small electrochemical cell employed for the SECM measurements consisted of a  
180 bronze sample of flat  $1.44 \text{ cm}^2$  area. Control on this area preventing electrolyte-metal contact at  
181 the sides of the sample was established once the target was embedded in epoxy resin (Buhler,  
182 Epoxyure<sup>TM</sup>) to avoid electrolyte penetration, and this was placed at the bottom of the small  
183 electrochemical cell facing upwards. The auxiliary and the reference electrodes were a platinum  
184 wire and an Ag/AgCl/KCl (sat.) electrode, respectively. Ferrocene-methanol (Fc-OH) was  
185 employed as redox mediator for the amperometric feedback operation of SECM.  $1 \text{ mM}$  Fc-OH  
186 was added to the test electrolytes, and the tip was biased at  $+0.50 \text{ V vs. Ag/AgCl/KCl (sat.)}$  to  
187 ensure the electro-oxidation of ferrocene-methanol under diffusion-controlled conditions.

188           Following concerns regarding the possible blockage of the microelectrode surface  
189 (fouling) by corrosion products arising from the reactions occurring at the copper alloy [51], the  
190 surface condition of the Pt microelectrode was continuously monitored and eventually  
191 regenerated. This effect was circumvented in this work by performing short-duration scans (5  
192 min for each 2-D measurements), and by mechanically polishing the SECM probe every time the  
193 control CV exhibited a distorted sigmoid shape. The short duration condition was achieved by  
194 adjusting the scan rate at  $25 \mu\text{m s}^{-1}$  with  $50 \mu\text{m}$  resolution, as a compromise to perform short-  
195 lasting scans providing surface information before eventual fouling of the microdisk, without  
196 excessively speeding the movement of the probe to avoid convective effects. It must be noticed  
197 that the procedure employed to assure the reproducibility of the Pt microelectrode was performed  
198 without removing it from the tip holder, and therefore its position with respect to the surface  
199 under study kept under control.

200

#### 201 *2.5. Chemical and morphological analyses*

202           The characterization of the bronze surface was performed after immersion of the  
203 electrodes during 24-h in the corrosive solutions both in the absence and in the presence of HCE  
204 at desired concentration. Then, the specimens were washed gently with water, carefully dried and  
205 characterized without any further treatment by SEM-EDS. SEM measurements were performed  
206 using a JEOL JSM 5600 LV microscope, while the chemical analysis of the surface was  
207 performed by EDS using an Oxford Instruments spectrometer (INCA 200 software). The energy  
208 of the acceleration beam was 15 kV.

209           The characterization of HCE was conducted by Fourier Transform-Infrared (FT-IR)  
210 spectroscopy, gas chromatography–mass spectrometry (GC-MS), and high-performance liquid  
211 chromatography, photo diode array detection (HPLC-PDA) measurements. FT-IR absorption  
212 spectrum of the horse chestnut extract was recorded in KBr pellet with a Bruker Vector 22 FT–  
213 IR spectrometer from  $4000$  to  $600 \text{ cm}^{-1}$ . GC-MS was recorded on Agilent 2010 PLUS Mass  
214 Spectrometer coupled with Gas Chromatograph equipped with a Carbowax type column ( $30 \text{ m} \times$   
215  $0.32 \text{ mm ID}$  and  $0.50 \mu\text{m}$  film thicknesses). Helium at a flow rate of  $0.7 \text{ mL min}^{-1}$  was used as  
216 the carrier gas, and  $1 \mu\text{L}$  sample was injected. The analysis was performed as follows: injector  
217 temperature  $250^\circ\text{C}$ , the ion source temperature  $220^\circ\text{C}$ , and the interface temperature  $250^\circ\text{C}$ . The  
218 column temperature program was the following: the initial temperature was  $40^\circ\text{C}$  and it was

219 maintained for 5 min, subsequently increased to 220°C at a rate of 4°C min<sup>-1</sup>, and then it was  
220 held at 220°C for 15 min. The electron impact (EI) was set at 70 eV. A mass range of 35–500  
221 *m/z* was recorded at one scan per second. The chemical species were identified using the Wiley  
222 Registry of mass spectra databases (WILEY Library 8 L).

223 The dark-brown solid resin (concentrated alcoholic extract of *Aesculus hippocastanum*)  
224 used in the present study (2 g of solid resin), was dissolved in 50 ml ethanol (80% v/v) to give a  
225 4% solution (m/v). The obtained extract was used for spectrophotometric determinations (total  
226 polyphenolic content and flavonoid content) and HPLC-PDA determinations of individual  
227 phenolics.

228 Total soluble phenolic compounds from the extract were determined with Folin-Ciocalteu  
229 reagent according to the method of Singleton *et al.* [52] with some modifications. A volume of  
230 0.5 mL extract, was placed in a glass tube and 2.5 mL Folin–Ciocalteu reagent (diluted 1:10) was  
231 added and after 5 min, 3 mL of 7.5% (w/v) sodium carbonate was also added. The tubes were  
232 incubated in the dark for 2 h at room temperature and the absorbance of the mixture was read at  
233 760 nm against a blank consisting of methanol, Folin–Ciocalteu reagent and sodium carbonate.  
234 For the calibration curve, a stock solution of gallic acid 1 mg mL<sup>-1</sup> was used, serial dilutions  
235 (0.005 – 0.1 mg mL<sup>-1</sup>) were made and subjected to the same protocol. The calibration curve  
236 equation for calculating the amounts of polyphenols was  $y=8.48752x+0.02576$ , with  $R^2=0.9965$ .  
237 The results were expressed as gallic acid equivalents.

238 The flavone/flavonol content was determined using a method adapted by Arvonet-Grand  
239 *et al.* [53] using a standard curve of quercetin (0.001 – 0.04 mg mL<sup>-1</sup>;  $y = 47.66539x - 0.01857$ ;  $R^2$   
240 = 0.99712). In brief, 3 mL of diluted extract was placed in a glass tube and the same amount of  
241 5% aluminium chloride was added, mixed thoroughly and placed in the dark for 30 min.  
242 Absorbance readings were made at 415 nm using a Pharmaspech UV–1700, Shimadzu  
243 spectrophotometer (Kioto, Japan) against a blank sample containing methanol and AlCl<sub>3</sub>  
244 solution. The flavonoid content was expressed as mg of quercetin equivalents. A Shimadzu LC-  
245 10ADVP system (Kioto, Japan), consisting of SCL-10AVP system controller, SPP-M20A  
246 Prominence Diode Array Detector, LC-10ADSP binary pumps, CTO-10AVP column oven and  
247 SIL-10AF autosampler, was used for separation of individual phenolics. Separation was carried  
248 out on a Supelcosil LC-18 column (250mm × 4.6mm, 5µm), using as mobile phases  
249 methanol:acetic acid:H<sub>2</sub>O 10:2:88 (solvent A) and methanol:acetic acid:H<sub>2</sub>O 90:3:7 (solvent B),



250 using the following linear gradient of A-B: 10 min, 85:15; 30 min, 50:50; 45 min, 15:85; 55  
251 min, 100:0 (total run time, 60 min). Phenolic acids and flavonoids chromatograms were  
252 registered at 254, 270, 320 and 340 nm. Co-chromatography with standards was also performed,  
253 for identification of phenolic compounds from the sample. The concentrations of each individual  
254 compound was determined based on external standard method, using calibration curves of each  
255 compound, after comparing the retention time and UV spectra with reference standards.

256

### 257 **3. Results and discussion**

#### 258 *3.1. Fourier transform infrared spectroscopy measurements, gas chromatography-mass* 259 *spectrometry and high-performance liquid chromatography characterization*

260

261 FTIR spectroscopy, GC-MS and HPLC were used to chemically identify the components  
262 of the HCE and their functional groups. The obtained GC-MS and HPLC-PDA chromatograms  
263 are shown in Figure 1. *Aesculus hippocastanum* seed extract contain a complex chemical  
264 composition, polysaccharides (both starches and non-starches), proteins, lipids, mineral salts,  
265 saponin also named escins, flavonoids and many minor components. The molecular structures of  
266 several organic compounds identified in HCE by GC-MS are listed in Table 1, depicting a  
267 complex chemical composition involving saturated and unsaturated aliphatic acids, esters,  
268 alcohols and heterocyclic derivatives.

269 As shown in Figure 1B, the ethanolic extract of horse chestnut also possess high amounts  
270 of biologically active compounds from the class of polyphenols and different classes of  
271 flavonoids (flavones/flavonols, flavanones/dihydroflavonols, or other phenols). The  
272 characteristic compounds identified in the horse-chestnut extract by HPLC-PDA and their  
273 concentrations are presented in Table 2. The total phenolic content of the alcoholic extract of  
274 horse chestnut was 2.53% and 1.01% flavone/flavonol content, similar to other studies [54,55].  
275 One phenolic acid was identified and quantified (3,4-dihydroxibenzoic acid) as well as six  
276 flavonoids (myricetin-3-rhamnozide, quercetin-3-glucozide, quercetin-rutinozide, quercetin-3-  
277 rhamnozide, quercetin and kaempferol). The highest amounts of flavonoids were two quercetin  
278 glycosides (quercetin-3-glucozide (114.99 ppm) and quercetin-3-rhamnozide (89.69 ppm).

279 The FTIR spectrum of the horse-chestnut extract is given in Figure 2. The most abundant  
280 compounds presented in HCE contain functional groups (i.e., hydroxyl, carbonyl, ester) and

281 heterocycles, as well as unsaturated rings, which could act as adsorption centres on metallic  
282 surfaces. Phenolic acids and flavonoids (both aglycones and glycosides), present this  
283 characteristic, due to the presence of hydroxyl groups and heterocycles from their structure.  
284 Broad absorption peak was found between 3000 and 3700  $\text{cm}^{-1}$  in the FTIR spectra,  
285 corresponding to the free and associated stretching vibration of OH groups from starches-based  
286 matrix, carbohydrate and other constituents from the HCE. The main ester and fatty acids  
287 responsible for the vibrations observed in the FT-IR spectrum include the symmetrical and  
288 asymmetrical stretching vibration of the alkyl units,  $\nu(\text{CH}_2)$  2854  $\text{cm}^{-1}$  and 2925  $\text{cm}^{-1}$ ; the  
289 bending vibration of the methyl units,  $\delta(\text{CH}_3)$  1465  $\text{cm}^{-1}$ ; the carbonyl stretching vibration at the  
290 expected position,  $\nu(\text{C}=\text{O})$  1744  $\text{cm}^{-1}$  and a characteristic vibration for ester  $\nu(\text{C}-\text{O})$  1376  $\text{cm}^{-1}$ .  
291 Finally, the unsaturated fatty acids methyl linoleate and methyl elaidate and others seem to be  
292 responsible for the stretching vibration  $\nu(\text{C}=\text{C})$  1651  $\text{cm}^{-1}$ .

293

### 294 3.2. Corrosion studies

#### 295 3.2.1. Polarization curve measurements

296 The polarization curves for bronze were recorded in 0.2  $\text{g L}^{-1}$   $\text{Na}_2\text{SO}_4$  + 0.2  $\text{g L}^{-1}$   
297  $\text{NaHCO}_3$  (pH 5) solution with and without HCE. The effect of HCE concentration on the  
298 polarisation behaviour of bronze was first recorded at 298 K and it is presented in Figure 3. It  
299 was found that the addition of HCE to the corrosive solution shifted both the cathodic and the  
300 anodic curves towards lower current densities values as compared to those obtained in the  
301 inhibitor-free solution. This trend was more pronounced as the concentration of HCE increased  
302 from 0.1  $\text{g L}^{-1}$  to 0.5  $\text{g L}^{-1}$ ; beyond that, the current density values slightly increase at higher  
303 concentrations of inhibitor, but they remained lower with respect to uninhibited solution.

304 Compared to the anodic curves, the shift of the cathodic curves with HCE concentration  
305 is less apparent. Thus, it can be inferred that HCE is able to retard to some extent both  
306 electrochemical reactions, *i.e.* the cathodic oxygen reduction and the anodic bronze dissolution,  
307 with a predominant control on the anodic reaction.

308 Quantitative information on the kinetics of the corrosion process was derived by  
309 determining the characteristic electrochemical parameters from the Tafel extrapolation of the  
310 polarization curves, namely the corrosion current density ( $j_{\text{corr}}$ ), the corrosion potential ( $E_{\text{corr}}$ ),

311 and the cathodic ( $-\beta_c$ ) and anodic ( $\beta_a$ ) Tafel slopes, given in Table 3. Inhibition efficiency ( $z$ )  
312 values calculated according to equation (1) are also presented in Table 3.

$$z (\%) = \frac{j_{\text{corr}}^0 - j_{\text{corr}}}{j_{\text{corr}}^0} \times 100 \quad (1)$$

314 where  $j_{\text{corr}}$  and  $j_{\text{corr}}^0$  are the corrosion current density values determined in the test electrolytes  
315 with and without HCE, respectively.

316 The results given in Table 3 show a decrease of  $j_{\text{corr}}$  values in the presence of HCE, and  
317 the lowest value was obtained in the solution containing 0.5 g L<sup>-1</sup> HCE. By increasing the HCE  
318 concentration, the  $j_{\text{corr}}$  values are slightly higher than in the case of 0.5 g L<sup>-1</sup>. Accordingly, the  
319 inhibition efficiency attains its maximum value of 87.5% in the presence of 0.5 g L<sup>-1</sup> HCE. As  
320 shown in Table 3, the addition of higher HCE concentrations up to 1 g L<sup>-1</sup> did not improve the  
321 inhibition efficiency for bronze protection.

322 The decrease of  $j_{\text{corr}}$  values in the presence of HCE might be ascribed to the adsorption of  
323 the organic compounds from HCE on bronze, through the oxygen atoms in their functional  
324 groups (*i.e.* O-H, C-OH, C=O) and the aromatic rings with the consequent formation of an  
325 insulating layer, which blocks the active reaction sites on the metal surface.

326 No definite trend was observed in the shifts of  $E_{\text{corr}}$  values at different HCE  
327 concentrations. However, all the displacements were smaller than 85 mV, which supports the  
328 idea that the horse chestnut extract behaves as a mixed-type inhibitor. It is also worth mentioning  
329 that  $\beta_a$  values substantially increased when HCE was added to the corrosive medium, while  
330 simultaneously the  $-\beta_c$  values were less affected by the presence of the inhibitor. These changes  
331 of the Tafel slopes further reveal that HCE suppresses both electrochemical reactions by  
332 adsorbing on the bronze surface, but the anodic suppression plays a dominant role in this process  
333 [26].

334 The effect of temperature was further investigated. Since temperature is an important  
335 factor that affects the metals corrosion behaviour and change the adsorption strength of the  
336 inhibitors on metal surfaces [33,42], the effect was next studied using polarization  
337 measurements. Several changes might occur on the metallic surface with temperature increasing,  
338 such as rapid etching and desorption of the inhibitor or even the decomposition of the inhibitor  
339 [56]. In order to gain more information about the type of adsorption and the anticorrosive  
340 effectiveness of the HCE at higher temperatures, polarization measurements were performed in

341 0.2 g L<sup>-1</sup> Na<sub>2</sub>SO<sub>4</sub> + 0.2 g L<sup>-1</sup> NaHCO<sub>3</sub> (pH 5) solution in the absence and in the presence of HCE  
 342 at various temperatures in the range from 298 K to 328 K. The solution pH slightly varied when  
 343 increasing the temperature. Thus, experiments conducted at 328 K showed pH 5.45, whereas the  
 344 inhibitor-containing solutions exhibited pH 5.18. Such minor pH variations did not disturb  
 345 significantly the expected linearity in the Arrhenius plot. The experimental results are depicted in  
 346 Figures 3 and 4, and the values of the associated electrochemical parameters from Tafel  
 347 extrapolation and  $z(\%)$  for all the HCE concentrations are summarized in Tables 3 and 4.

348 Table 4 shows that the temperature raising leads to a decrease of the  $j_{\text{corr}}$  values for  
 349 uninhibited and inhibited solutions, as well. However, the values of  $j_{\text{corr}}$  obtained in the presence  
 350 of HCE at high temperatures are lower with respect to the blank solution, indicating that HCE  
 351 exhibits some inhibiting properties at all studied temperatures.

352 The anticorrosive efficiency of HCE on bronze decreases gradually with the temperature  
 353 increase (Tables 3 and 4). Nevertheless, in the presence of the ‘optimum’ concentration of  
 354 inhibitor (0.5 g L<sup>-1</sup>), the  $z(\%)$  value is rather high even at 328 K, accounting around 73.1%. The  
 355 increase of the corrosion rates with the temperature was noticed for other natural corrosion  
 356 inhibitors [32–36,39,40,42]. This behaviour could be explained by partial desorption [32–  
 357 34,36,39,40] or even decomposition of the HCE at high temperatures, resulting in a lower  
 358 coverage of the bronze surface.

359 To further understand the kinetics of corrosion inhibition process in the presence of HCE,  
 360 the activation parameters were calculated from Arrhenius and transition state equations [33,56]:

$$361 \quad i_{\text{corr}} = k \exp\left(-\frac{E_a}{RT}\right) \quad (2)$$

$$362 \quad i_{\text{corr}} = \frac{RT}{N\hbar} \exp\left(\frac{\Delta S_a}{R}\right) \exp\left(-\frac{\Delta H_a}{RT}\right) \quad (3)$$

363 where  $k$  is the Arrhenius pre-exponential factor,  $E_a$  the activation corrosion energy,  $R$  the  
 364 universal gas constant,  $T$  the absolute temperature,  $h$  the Planck’s constant,  $N$  the Avogadro’s  
 365 number,  $\Delta S_a$  the entropy of activation,  $\Delta H_a$  the enthalpy of activation, and  $j_{\text{corr}}$  is the corrosion  
 366 current density, which is directly related to rate of metal dissolution reaction [56,57].

367 Figure 5A depicts the Arrhenius plots for bronze corrosion in the absence and in the  
 368 presence of HCE at different concentrations. The calculated  $E_a$  values are listed in Table 4.  
 369 Inspection of the data in Table 4 evidences that  $E_a$  values obtained in the presence of HCE are

370 higher than in its absence, which could be associated to a physical adsorption process of the  
371 inhibitor on the bronze surface that occurs in the first stage, in accordance with previously  
372 reported results [32–34,36,39,40]. Hence, the presence of the inhibitor kinetically hinders the  
373 bronze degradation due to the eventual adsorption of the organic compounds, which prevent the  
374 occurrence of the electrochemical reactions at the surface. According to the literature [33,34,39],  
375 the increase in  $j_{\text{corr}}$  in warmer environments might be attributed to a decrease of the inhibitor  
376 adsorption on the metallic surface as the temperature increases, resulting in larger metal areas  
377 exposed to the corrosive solution.

378 On the other hand, Figure 5B shows the plots of  $\ln(j_{\text{corr}}/T)$  against  $1/T$  for the blank and  
379 with different concentrations of inhibitor. Straight lines were obtained with a slope of  $(-\Delta H_a/R)$   
380 and an intercept of  $[\ln(R/Nh) + \Delta S_a/R]$ , from which the values of  $\Delta H_a$  and  $\Delta S_a$  were calculated  
381 and included in Table 4. The positive signs of the activation enthalpies,  $\Delta H_a$  indicate that the  
382 dissolution process of bronze is endothermic in nature [56], whereas the negative values for  $\Delta S_a$   
383 in uninhibited and inhibited solutions indicate that the formation of the activation complex in the  
384 rate determining step represents an association rather than a dissociation step, meaning that a  
385 decrease in disorder takes place during the course of the transition from reactants to the activated  
386 complex [32].

387

### 388 3.2.2. *Electrochemical impedance spectroscopy measurements*

389 In order to assess the time evolution of the inhibitive layer performance of the HCE  
390 during time, EIS measurements were performed at different exposure periods up to 36 h in 0.2 g  
391  $\text{L}^{-1}$   $\text{Na}_2\text{SO}_4$  + 0.2 g  $\text{L}^{-1}$   $\text{NaHCO}_3$  (pH 5) solution without and with the addition of HCE at various  
392 concentrations. The first impedance measurement was carried out after 1-h stabilization period at  
393 298 K. Subsequently, the impedance spectra were collected every 2 h.

394 Figure 6 shows typical examples of impedance spectra represented as Nyquist diagrams  
395 and Bode plots measured on the corroding bronze electrode at different immersion times in the  
396 uninhibited bronze and in bronze exposed to the HCE-containing solutions. The impedance  
397 diagrams are characterized by a flattened semi-circular shape with capacitive loops in the entire  
398 frequency domain. The diameters of the capacitive loops obtained in the presence of HCE were  
399 larger than for uninhibited solution, which confirms the anticorrosive properties of the studied  
400 inhibitor.

401 The impedance spectra of bronze obtained in the blank electrolyte consisted of two-  
 402 relaxation constants, and the equivalent electrical circuit composed of two ladder parallel  $R$ - $Q$   
 403 circuits depicted in Figure 7A was used to reproduce the experimental data and to extract the  
 404 corresponding  $R$ - $Q$  parameters. As the loops in the impedance diagrams are depressed  
 405 semicircles, constant phase elements (CPE), represented by the terms  $Q$  and  $n$ , were used instead  
 406 of capacitances to compensate for the surface roughness and other inhomogeneities, the  
 407 adsorption of the inhibitor and the variations in the composition and properties of the surface  
 408 layers. The impedance of the CPE is defined as [58]:

$$409 \quad Q = Z_{\text{CPE}(\omega)} = [C(j\omega)^n]^{-1} \quad (3)$$

410 where  $Q$  is the constant of the CPE element,  $j$  is the imaginary number,  $\omega$  is the angular  
 411 frequency and  $n$  is the exponent which defines the character of frequency-dependence ( $-1 \leq n \leq$   
 412  $1$ ).

413 The obtained fitted curves have been plotted as crosses in the Nyquist diagrams and lines  
 414 in the Bode diagrams, and they are shown together with the experimental data represented by  
 415 symbols in the spectra shown in Figure 6. It can be observed that the experimental and the  
 416 calculated impedance data superimposed almost perfectly on each other, demonstrating the  
 417 validity of the equivalent electrical circuits adopted for the simulation of the electrochemical  
 418 impedance data. In our study, the values of the  $n$  exponent in the CPE analytical expressions  
 419 used for fitting the depressed features of the experimental impedance ranged 0.50 - 0.99, an  
 420 interval similar to other reported results [27], reflecting intermediate behaviour between a  
 421 capacitor and a resistor.

422 By following several reported studies [13,19,59], a physical interpretation of the circuit  
 423 elements can be given as follows:  $R_e$  is the solution resistance,  $R_{ct}$  and  $Q_{dl}$  are parameters  
 424 describing the charge transfer process at the bronze/electrolyte interface, while the low  
 425 frequency elements,  $R_F$  and  $Q_F$  refers to an oxidation-reduction process taking place at the  
 426 electrode surface, involving the surface corrosion products (possibly related to the redox reaction  
 427 between Cu and Cu(I)).

428 In the presence of HCE, three capacitive loops, though badly separated each other are  
 429 necessary for the computer fitting of experimental data. The corresponding equivalent circuit  
 430 with three-time constants given in Figure 7B contains an additional  $R_f$ - $Q_f$  couple that is observed  
 431 in the high-frequency domain and can be ascribed to the formation of a thin surface film by the

432 adsorbed inhibitor.  $R_f$  represents the resistance towards the access of ions through the pores of  
433 the surface film, and  $Q_f$  corresponds to the capacitance of the surface film. The values of the  
434 pseudo-capacitances ( $C$ ) associated with each of the CPE's were recalculated using the equation  
435 [60]:

$$C = (R^{1-n}Q)^{1/n} \quad (4)$$

436  
437 where  $R$  and  $Q$  were taken from the values of the corresponding time constants.

438 Figure 8 shows the variation of  $R$ - $C$  parameters from each time constant with respect to  
439 HCE concentration and the immersion time, respectively. It should be mentioned that the  
440 evolution of the  $R$  and  $C$  parameters determined in the solution containing  $1 \text{ g L}^{-1}$  HCE followed  
441 a rather similar behaviour to those obtained in the presence of  $0.75 \text{ g L}^{-1}$  HCE and, for the sake  
442 of simplicity, they were further neglected from the subsequent discussions. Considering each  
443 time constant in turn, the following observations can be derived:

444 (1)  $R_f$ - $C_f$  couple. The addition of  $0.1 \text{ g L}^{-1}$  HCE to the test solution originated a gradual  
445 increase of the film resistance values from ca.  $0.19 \text{ k}\Omega \text{ cm}^2$  to  $1.3 \text{ k}\Omega \text{ cm}^2$  during the first 14-h of  
446 exposure (cf. Figure 8A), whereas the film capacitance decreased and attained the lowest value  
447 of  $1.3 \mu\text{F cm}^{-2}$  (see Figure 8B). After that period, the values of  $R_f$  remained almost constant up to  
448 36-h immersion and  $C_f$  increased slightly towards the end of the experiment. These results are  
449 consistent with the formation of a thin protective film, likely due to the progressive adsorption of  
450 HCE components on the bronze surface, through their available adsorption centres that were  
451 identified using FTIR, GC-MS and HPLC measurements. A gradual thickening of the surface  
452 film takes place within the first 14-h of exposure, which makes the ionic conduction through this  
453 layer more difficult. The increase of HCE concentration to  $0.5 \text{ g L}^{-1}$  resulted in a significant  
454 decrease of  $C_f$  values at the initial stages of immersion, while simultaneously the film resistance  
455 was about 40 times higher after 1-h of exposure (namely,  $R_f = 7.6 \text{ k}\Omega \text{ cm}^2$ ) compared to the  
456 value of  $R_f$  determined in the solution containing  $0.1 \text{ g L}^{-1}$  HCE.

457 In the case of  $0.5 \text{ g L}^{-1}$  HCE, the adsorption of the inhibitor on the bronze surface was  
458 facilitated, allowing the formation of a less permeable surface film within 1-h exposure. As time  
459 elapsed, the surface film grew slowly and progressively became more compact and resistant  
460 towards the passage of the metallic ions through the pores of the film. Nevertheless, the  
461 permeability of this surface film towards charged species decreased in some extent after 14-h of  
462 exposure, as demonstrated by the small decrease of the  $R_f$  values at this stage. A further increase

463 of HCE concentration to  $0.75 \text{ g L}^{-1}$  did not contribute to improve the resistance of the surface  
464 film; that is, the corresponding  $R_f$  values were lower than those obtained in the presence of  $0.5 \text{ g}$   
465  $\text{L}^{-1}$  HCE. Although some film thickening took place on the bronze surface exposed to the  
466 solution containing  $0.75 \text{ g L}^{-1}$  of the inhibitor, its protective characteristics deteriorated at long  
467 immersion times.

468 (2)  $R_{ct}$ - $C_{dl}$  couple. As shown in Figure 8C, the values of the charge transfer resistance,  $R_{ct}$ ,  
469 increased with HCE concentration up to  $0.5 \text{ g L}^{-1}$ , and they slightly decreased above this  
470 concentration. A progressive augmentation of  $R_{ct}$  values with the immersion time was noticed  
471 within the first 14-h of exposure, disregarding the inhibitor concentration. Beyond this time, a  
472 decreasing trend of  $R_{ct}$  values could be observed in Figure 8C for all the considered HCE  
473 concentrations. However, the decay of  $R_{ct}$  was more pronounced in the presence of  $0.75 \text{ g L}^{-1}$   
474 HCE. The results proved the ability of HCE to hinder the charge transfer reaction. Its inhibitive  
475 properties were initially enhanced for some time, although they started to diminish at a slow pace  
476 for long exposures, and more particularly when the HCE concentration exceeded  $0.5 \text{ g L}^{-1}$ .

477 The double-layer capacitance,  $C_{dl}$  values were lower in the presence of HCE with respect  
478 to the uninhibited solution and gradually decreased during about 20-h of exposure; after that  
479 period, the values of  $C_{dl}$  remained almost constant until the end of the experiments, except for  
480 the solution containing  $0.75 \text{ g L}^{-1}$  (see Figure 8D). In this later case, the  $C_{dl}$  values increased at  
481 long immersion and attained values as high as those corresponding to the uninhibited solution.  
482 This decrease of  $C_{dl}$  could be attributed to a smaller exposed area directly in contact with the  
483 corrosive solution, on which the charge transfer reaction might occur, and/or to the progressive  
484 replacement of the water molecules by the adsorbed organic molecules with low dielectric  
485 constant within the double layer [27].

486 (3)  $R_F$ - $C_F$  couple. This couple is mainly attributed to the kinetics of a reversible redox  
487 process involving a surface species (*i.e.*  $\text{Cu}_2\text{O}$ ) accumulated during the corrosion process,  
488 according to a mechanism based on the following sequence of reactions [19]:



491 For all the studied HCE concentrations, the faradaic resistance,  $R_F$ , tended to increase  
492 with the immersion time during the first 10-14 h of immersion (cf. Figure 8E), in accordance  
493 with the corresponding variation of  $C_{dl}$  values (Figure 8D). As time elapsed, except for the



494 solution containing  $0.75 \text{ g L}^{-1}$  HCE,  $R_F$  attained an almost steady-state condition, with values 7 to  
 495 10 times greater than those obtained in the uninhibited solution. Simultaneously, the capacitances  
 496 associated to this process that were determined in the presence of HCE were lower than the  $C_F$   
 497 values obtained for the blank solution, as shown in Figure 8F. As expected, the greatest  $R_F$   
 498 values were obtained in the presence of  $0.5 \text{ g L}^{-1}$  HCE at all immersion times, while  $C_F$  attained  
 499 its lowest values at this HCE concentration as well.

500 The obtained results suggest that the adsorption of HCE stabilizes the corrosion products  
 501 formed on the surface, which became less susceptible to participate in the redox reaction  
 502 between Cu and  $\text{Cu}_2\text{O}$ . However, by increasing the HCE concentration to  $0.75 \text{ g L}^{-1}$ , the  
 503 electrochemical (faradaic) processes occurring at the bronze surface might eventually be  
 504 accelerated at longer exposure times [13], which would give rise to higher  $C_F$  values.

505 It is known [61] that in the presence of redox processes taking place on the metallic  
 506 surface, the polarization resistance,  $R_p$ , is better correlated with the corrosion rate than  $R_{ct}$ . Since  
 507 the film resistance,  $R_f$  is a non-faradic parameter, the polarization resistance  $R_p$  could be defined  
 508 as:

$$R_p = R_{ct} + R_F \quad (7)$$

510 The  $R_p$  values were used to calculate the inhibition efficiency,  $z$ , according to the  
 511 following equation:

$$z (\%) = \frac{R_p - R_p^0}{R_p} \cdot 100 \quad (8)$$

513 where  $R_p$  and  $R_p^0$  are the polarization resistances in solutions with and without HCE,  
 514 respectively. Figure 9 shows the time evolution of  $R_p$  and  $z$  values during the exposure to the  
 515 corrosive solutions in the absence and in the presence of HCE at different concentrations. The  
 516 polarization resistance increased with time and presented its highest values in solutions  
 517 containing  $0.5 \text{ g L}^{-1}$  HCE. Above this concentration, a decrease of the  $R_p$  values could be noticed,  
 518 particularly at longer immersion, as expected from the above-mentioned results.

519 After 1-h immersion, the anticorrosive effectiveness of the HCE is rather moderate, as  
 520 shown in Figure 9B. A gradual reinforcement of its inhibiting properties was noticed after about  
 521 14-h when  $z(\%)$  attained maximum values of 84.8%, 94.1% and 82.8% for HCE concentrations  
 522 of 0.1, 0.5 and  $0.75 \text{ g L}^{-1}$ , respectively. Although the inhibitive efficiencies of HCE decreased

523 slightly at longer immersions up to 36-h, this natural product offered acceptably lasting  
524 anticorrosive protection to bronze in  $0.2 \text{ g L}^{-1} \text{ Na}_2\text{SO}_4 + 0.2 \text{ g L}^{-1} \text{ NaHCO}_3$  (pH 5) solution.

525 Although the complex chemical composition of HCE makes rather difficult to assign its  
526 inhibiting action to a particular constituent or group of constituents, some preliminary EIS  
527 experiments were performed using the two main components identified in the HCE (cf. Tables 1  
528 and 2), namely quercetin and kaempferol. This choice was based on reports of corrosion  
529 inhibition effects provided by several plant extracts containing phenolic acids and flavonoids as  
530 chemical constituents [62]. Firstly, 12.5 ppm of quercetin were added to the blank test solution, a  
531 value close to the overall concentration of quercetin and its derivatives (i.e., 250 ppm) in  $0.5 \text{ g}$   
532  $\text{L}^{-1}$  HCE. It was found that the appearance of the treated bronze surface resembled that developed  
533 in the corresponding HCE-containing solution, whereas the measured EIS data (not shown  
534 here) followed quite closely the impedance diagram of  $0.5 \text{ g L}^{-1}$  HCE although with slightly  
535 smaller total impedances. Upon the increase of the quercetin concentration up to 25 ppm, the  
536 impedance increased closer to that of the HCE-containing solution, but precipitation of the  
537 compound from the solution occurred in less than 2 h, even if ethanol was employed for  
538 dissolution. This feature effectively prevented us from testing higher concentrations of quercetin.  
539 On the other hand, in a similar experiment involving kaempferol, no inhibiting effect could be  
540 observed against the corrosion of bronze in simulated acid rain. In summary, compounds of the  
541 quercetin group may be considered to contribute to the inhibition corrosion effect for bronze  
542 reported in this work, but they may produce such effect together with other substances, and the  
543 eventual occurrence of synergistic effects could not be discarded at this stage.

544

### 545 3.3. SEM-EDS characterization

546 Figure 10 shows SEM micrographs and the corresponding EDS spectra of bronze  
547 surfaces after 36 h exposure to  $0.2 \text{ g L}^{-1} \text{ Na}_2\text{SO}_4 + 0.2 \text{ g L}^{-1} \text{ NaHCO}_3$  (pH 5) solution in the  
548 absence and presence of  $0.5 \text{ g L}^{-1}$  HCE. It should be noted that the parallel features observable  
549 on the bronze surfaces after exposure to the test solutions without and with HCE originated from  
550 the prior surface preparation step that originated grinding scratches.

551 It can be seen in Figure 10A that the bronze surface appeared to be rough and covered  
552 with a layer of corrosion products after 36-h exposure to the uninhibited corrosive solution. The  
553 EDS analysis in Figure 10C revealed high amounts of oxygen on the bronze surface, in addition

554 to the major elements (Cu and Sn). Hence, the corrosion products would be mainly metal oxy-  
555 hydroxides.

556 The morphology of the bronze surface after its immersion in the solution containing 0.5 g  
557 L<sup>-1</sup> HCE was significantly different (see Figure 10B). A marked decrease of the surface  
558 roughness occurred in the presence of the inhibitor, and it must be regarded to result from HCE  
559 adsorption on the metallic surface. Although some oxides are still present on the bronze surface  
560 treated with 0.5 g L<sup>-1</sup>HCE as shown in the EDS spectra shown in Figure 10D, a significant  
561 decrease of the oxygen peak could be noticed when the bronze was in contact with the HCE, thus  
562 confirming the corrosion inhibition effect occurring in the investigated experimental conditions.  
563 However, the persistence of oxides on the bronze surface after immersion in the HCE-containing  
564 solution is reasonable because the inhibiting efficiency of HCE is smaller than 100%.

565

#### 566 3.4. SECM analysis

567 To investigate the reactivity of the metal surface and the tendency of bronze to electron  
568 transfer with spatial resolution, a random area of 500 μm × 500 μm was chosen on the bronze  
569 substrate and 2-D scans were recorded in the amperometric feedback operation mode in the same  
570 location. Ferrocene-methanol was used as redox mediator, and the Pt microelectrode tip was  
571 polarized at +0.50 V vs. Ag/AgCl/KCl(sat.) for the diffusion-controlled oxidation of this species.

572 Selected SECM images recorded at different immersion times in the inhibitor-free  
573 solution are shown in Figure 11. In them, the faradaic current measured at the tip,  $i$ , was  
574 normalized with respect to the limiting current  $i_{lim}$  recorded before each scan acquisition while  
575 the tip was placed in the bulk of the solution. Therefore, the  $I = i/i_{lim}$  values greater than 1  
576 evidenced the appearance of a positive feedback effect related to the surface exhibiting a  
577 combination of conductive behaviour with kinetic ability to allow the regeneration of the redox  
578 mediator following electron transfer from the substrate. In contrast, regions that delivered  
579 normalized current values smaller than 1 reflected predominance of negative feedback behaviour  
580 and, therefore, showed less surface reactivity. The surface is clearly heterogeneous, but positive  
581 feedback is predominant over a great section of the scanned area (yellow and red coloured), thus  
582 reflecting an electrochemically-active surface in the absence of the inhibitor. In addition, from a  
583 qualitative inspection of the images, the evolution of the SECM scan acquisition showed a  
584 greater number of active sites after longer exposure times, which suggests an increase in the

585 conductivity and the reactivity of the surface within the first two hours of immersion. Notorious  
586 corrosion phenomena occurred after this time in the aggressive environment, so the experimental  
587 series was stopped.

588 The behaviour observed in Figure 12 for a bronze sample immersed in the test solution  
589 containing HCE was different from that already described in the blank electrolyte. In this case, a  
590 concentration of  $0.5 \text{ g L}^{-1}$  was chosen for the *in situ* SECM experiments based on its higher  
591 inhibiting efficiency according to the potentiodynamic polarization and impedance  
592 measurements described above. Although the scan shown in Figure 12A, which was recorded  
593 after 29 min immersion, shows a mostly active surface similar to that in the inhibitor-free  
594 conditions (see Figures 11A and 11B), the positive feedback effect was hardly observed after 42  
595 min (cf. Figure 12B) and even longer immersion times (*i.e.* Figures 12C-D). Conversely, the  
596 imaged areas mostly exhibited the insulating-type behaviour and the negative feedback effect,  
597 reflecting the formation of a non-reactive layer that progressively blocked the active sites  
598 available for the electron donation needed in the regeneration of the redox mediator. Ultimately,  
599 almost the entire surface behaved as an insulator, and purely negative feedback effect was  
600 observed after 150 min (Figure 12D). In this stage, the formation of a sufficiently protective  
601 inhibitory surface derived in the effective hindrance of the diffusion of the mediator to the tip as  
602 only surface feature influencing the SECM response, hence only topographic information can be  
603 extracted from the SECM images.

604 Quantitative kinetic information on the surface tendency towards electron donation is  
605 accessible by recording the tip current while the tip is moved towards the investigated sample  
606 surface at some selected location [63]. The resulting probe approach curve (PAC) provides  
607 information about constant rate of the heterogeneous electron transfer for the reduction at the  
608 metal substrate of the ferrocinium species, which results from the oxidation of the redox  
609 mediator at the tip. The 2-D scans in Figures 11 and 12 confirmed that the constant rate changed  
610 dynamically and heterogeneously throughout the bronze surface. This dynamic behaviour was  
611 studied at the randomly chosen location corresponding to the (0,0) origin of the maps in Figures  
612 11 and 12. The resulting Z-approach curves are shown in Figure 13 for the sequence of PACs  
613 recorded at different elapsed times during the immersion of the samples in the inhibitor-free and  
614 the HCE-containing solution, respectively.

615 In the blank solution containing  $0.2 \text{ g L}^{-1}\text{Na}_2\text{SO}_4 + 0.2 \text{ g L}^{-1}\text{NaHCO}_3 + 1 \text{ mM}$  ferrocene-  
616 methanol (pH 5), an almost constant positive feedback behaviour typical of an electrochemically  
617 active surface was observed throughout the entire experimental series (see Figure 13A). On the  
618 contrary, when the same evolution was investigated in the presence of the HCE, the initial  
619 positive feedback diminished with the elapse of time as seen in Figure 13B, which evidences  
620 mixed positive-negative feedback behaviour. The limiting purely positive and negative feedback  
621 effects are also shown in the figure for the sake of comparison. However, a rather different  
622 dynamic evolution trend was recorded when selecting a different location on the bronze surface  
623 at which the Z-approach curves were recorded. For instance, Figure 13C shows the results  
624 obtained when the approach curves were performed at  $100 \mu\text{m}$  far from the origin in the Y  
625 direction (a location indicated by a green arrow in Figure 12A), which corresponded to a largely  
626 inactive region from the beginning of the experiment. In both cases, the PACs ultimately  
627 described purely negative feedback behaviour after 21-h immersion, regardless of the location in  
628 the surface.

629 Using well-established mathematical simulations for the approach curves in SECM  
630 experiments, and taking in account the geometry of the tip, the progressive evolution from  
631 positive to negative feedback in Figure 13B resulted in the calculation of values for the kinetic  
632 constant for the electron transfer at the selected locations on the substrate [63]. In the  
633 calculations, a diffusion coefficient of  $7.60 \times 10^{-6} \text{ cm}^2 \text{ s}^{-1}$  was used for the redox mediator [64],  
634 and the results are listed in Table 5. It is found that the evolution of the blocking effect of the  
635 inhibitory layer can be expressed in terms of hindered electron transfer by ca. 70%, *i.e.*, changing  
636 from  $7.3 \times 10^{-3}$  to  $2.1 \times 10^{-3} \text{ s}^{-1}$ . However, given the great surface heterogeneity of the system, these  
637 results reflect solely the evolution of single random locations, and they should be considered  
638 rather as semi-quantitative information instead of precise quantitative parameters describing the  
639 tendency of the whole surface.

640 The dynamic evolution of the SECM scans observed in Figures 11 and 12 can be  
641 correlated with the surface conductivity distribution and related protectiveness of the surface  
642 layers. In the absence of the inhibitor, the main phenomena involved in this evolution are the  
643 formation and dissolution of semiconductive oxide patinas, which seems to be predominant  
644 according to the high oxygen content monitored from the post-mortem EDS evaluation (cf.  
645 Figure 10C). As result of the treatment with the HCE inhibitor, the EDS observations did not

646 show an extensive formation of copper oxide, so the formation of patinas cannot account for the  
647 corrosion protection effect. The protection must stem from the adsorption of HCE on the bronze  
648 or the precipitation of metal cations with the complexing species, which occur heterogeneously  
649 within the first 1-2 hour immersion according to observations of SECM.

650 The dynamics of the evolution of the surface conductivity, resulting from the formation  
651 of patinas in inhibitor-free solution and for inhibitor-containing layers in the presence of HCE,  
652 can be analysed quantitatively from histograms depicting the distribution of the values of  
653 normalized current recorded in the scans shown in Figures 11 and 12. Figure 14A shows the  
654 histograms obtained for the analysis of the data recorded in inhibitor-free and HCE-containing  
655 solutions after 23-29 min immersion, whereas Figure 14B shows the corresponding analysis after  
656 70-min. The average value of the Gaussian distributions with their standard deviations  $\sigma$  are  
657 plotted against the immersion time in Figure 14C for both electrolyte solutions. The position of  
658 the Gaussian peaks did not differ much between the two electrolyte solutions at the beginning of  
659 the immersion, although it significantly decayed asymptotically with time only when the HCE  
660 was present. In the blank solution, the Gaussian peak position remained rather stable with values  
661 greater than unity for the normalized current value, showing a predominant and stable positive  
662 feedback behaviour overall. It is also noteworthy that the standard deviation increased with time  
663 in the absence of the inhibitor, evidencing a predominantly reactive substrate that exhibited a  
664 greater heterogeneity as the exposure time elapsed. Conversely, the standard deviation in the  
665 HCE-containing solution did not vary significantly, reflecting a constantly heterogeneous surface  
666 deactivation that actually affected the entire exposed surface in a similar manner throughout it.  
667 This deactivation may actually result from a convolution of the formation of the oxide patinas  
668 and the inhibitor adsorption. However, the remarkably different behaviour observed for bronze  
669 immersed in each test electrolyte, in terms of average current and deviations, suggests that the  
670 decreasing tendency attained upon exposure to HCE-containing media is more likely supported  
671 by the inhibiting effect, rather than the copper oxide development.

672 The asymptotic trend observed for the mean current decrease in the inhibited bronze  
673 system can be correlated with the kinetics of the protective layer formation, as it reflects the  
674 general blockage of the surface with the inhibitive film. This blockage effect stems from the  
675 overall interaction of the substances present in the extract (Tables 1 and 2), with the metal  
676 surface. Each of these components may exhibit different adsorption mechanisms and rates,

677 eventually influenced by synergistic effects (positive or negative). This is regarded as a frequent  
678 drawback when investigating the inhibitive effect of plant extracts due to the multiple  
679 compounds present in the matrix [65]. It must be noticed that the present study aimed to explore  
680 and demonstrate the ability of SECM to provide quantitative information on the overall  
681 adsorption procedure, addressing the dominant adsorption mechanism of the components in the  
682 inhibitive extract. Further investigation would be needed to provide insights on the single  
683 molecules or mixtures with major role on the adsorption and inhibitive effect and their  
684 adsorption mechanisms. However, concerns arise when considering any eventual separation of  
685 components from the extract for their more efficient application as inhibitor, since such strategy  
686 may compromise the ease and ecology of the direct use of the extract for corrosion protection, in  
687 the event of industrial-scale application.

688 The surface coverage by the adsorbed species could be expected to obey Langmuir  
689 isotherm [32,35,39,40], resulting in the surface coverage  $\theta$  evolving with immersion time  $t$   
690 according to:

$$691 \quad \theta(t) = K' [1 - \exp(-k_{\text{obs}}t)] \quad (9)$$

692 where  $K'$  and  $k_{\text{obs}}$  are constants depending on the adsorption and desorption rate constants and  
693 the concentration of the inhibitor.

694 The current models for the theoretical estimation of the normalized current values  
695  $I = i/i_{\text{lim}}$ , measured at the tip while performing the scans upon feedback behaviour, depict a  
696 complex mathematical dependence on several experimental variables, namely the kinetic rate  
697 constant of the electron transfer at the surface, the tip-to-substrate distance, the probe geometry  
698 and the diffusion coefficient of the redox couple [63]. Among them, the only parameter which  
699 depends on the surface properties is the kinetic rate constant  $k$ , which may be expressed as  
700 normalized magnitude  $\Lambda$ , as follows [66]:

$$701 \quad \Lambda = \frac{ka}{D} \quad (10)$$

702 where  $a$  is the radius of the microelectrode and  $D$  the diffusion coefficient of the redox mediator.  
703 Bard and co-workers proposed a linear correlation between the kinetic rate constant  $k$  and surface  
704 coverage, obtained using SECM in feedback mode for the investigation of mono- and bilayers  
705 deposited on gold surfaces [67]:

$$k = \frac{4(1 - \theta)D}{\pi R_d} \quad (11)$$

706 where  $R_d$  relates with the dimensions of the pinholes and pores in the layer. Combining equations  
 707 (9) to (11), we obtain the following expression:  
 708

$$A = \frac{4a}{\pi R_d} - \frac{4a}{\pi R_d} K' + \frac{4a}{\pi R_d} K' \exp[-k_{\text{obs}} \cdot t] \quad (12)$$

709  
 710 The values of  $A$  can be obtained by establishing a mathematical correlation from the  
 711 average  $I$  values in the Gaussian fit (Figure 14A and B), providing that the remaining parameters  
 712 are known. Although some concerns may arise from the probe geometry (namely, for  $Rg$  greater  
 713 than 20) as not being optimal for such calculation, systematic errors were not expected to exceed  
 714 10% at small tip-substrate distances. Therefore, considering the experimental parameters, the  
 715 normalized distance may be considered that providing the minimum limiting current  $I = 0.774$ ,  
 716 average value measured after 1260 min immersion when purely negative feedback is attained.  
 717 This current is obtained for  $L = 1.12$ , that is, 1.12 times the radius of the microelectrode (around  
 718  $7 \mu\text{m}$ ). With all these experimental parameters estimated, the  $A$  values have been calculated and  
 719 displayed in Figure 14D, along with the exponential tendency. The fitting procedure provides a  
 720 satisfactory correlation ( $R^2 = 0.98502$ ) with the following parameters:  $k_{\text{obs}} = 0.0136 \text{ min}^{-1}$  (or  
 721  $k_{\text{obs}} = 2.27 \times 10^{-4} \text{ s}^{-1}$ ); and  $K' = 0.853$ . These values allow the estimation of the adsorption and  
 722 desorption rate constants [68–70]:

$$k_{\text{obs}} = k_a C_{\text{HCE}} + k_d \quad (13)$$

$$K' = \frac{C_{\text{HCE}}}{C_{\text{HCE}} + \frac{k_a}{k_d}} \quad (14)$$

724  
 725 where  $C_{\text{HCE}}$  is the concentration of the adsorbed species. In order to provide appropriate  
 726 thermodynamic data, an average molecular weight must be estimated taking into account the  
 727 relative abundance of the compounds identified in Tables 1-2. For the current calculations, a  
 728 value of  $263.1 \text{ g mol}^{-1}$  was adopted. Hence,  $C_{\text{HCE}}$  is taken as  $1.90 \times 10^{-3} \text{ mol L}^{-1}$ , although it is very  
 729 unlikely that all the organic compounds in the mixture would promote inhibitive effect. By  
 730 solving this system of equations, the following apparent kinetic rate constants were obtained as  
 731 results:  $k_a = 0.102 \text{ s}^{-1} \text{ mol}^{-1} \text{ L}$ ,  $k_d = 3.33 \times 10^{-5} \text{ s}^{-1}$ . Adsorption rate constant is significantly greater  
 732 than other values reported with corrosion inhibitors used for copper as obtained with kinetic  
 733 studies done with electrochemical quartz microbalance, whereas desorption occurs at much



734 slower pace [69,70]. The equilibrium constant and resulting free energy for the adsorption-  
735 desorption process are given by:

$$736 \quad K_{eq} = \frac{k_a}{k_d} \quad (14)$$

$$737 \quad \Delta G = -RT \ln(K_{eq}) \quad (15)$$

738 In this way,  $K_{eq} = 3.06 \cdot 10^3 \text{ mol}^{-1} \text{ L}$ , and  $\Delta G = -19.9 \text{ kJ mol}^{-1}$  apparent values were obtained, in  
739 very good agreement with results estimated from EIS measurements after 1 hour exposure. These  
740 results account nearly half those encountered for not eco-friendly inhibitors adsorbed on bronze,  
741 typically between  $-30$  and  $-40 \text{ kJ mol}^{-1}$  [71–73]. Hence, promising values supporting  
742 physisorption processes were obtained, as expected for the interaction of bronze with organic  
743 molecules with oxygen as only heteroatom. Although a complete kinetic model accurately  
744 considering all the experimental conditions and current-influential features, including surface  
745 coverage, is still needed, the achieved results are acceptable under the expected values, and they  
746 demonstrate the efficiency of the chestnut extract as a good and fast inhibitive substance for the  
747 protection of bronze, with great tendency towards the adsorption of the inhibiting surface films  
748 in contrast to their desorption. To the best of our knowledge, this is the first time that  
749 thermodynamic and kinetic parameters were obtained from the analysis and evaluation of SECM  
750 experimental data for metal-inhibitor systems governed by an adsorption-desorption process.

751

#### 752 **4. Conclusions**

753 In the present work, the inhibitive behaviour of the ethanolic extract of horse chestnut  
754 seeds (*Aesculus hippocastanum L.*) on bronze in a weakly acidic aqueous environment simulating  
755 an acidic rain ( $0.2 \text{ g L}^{-1} \text{ Na}_2\text{SO}_4 + 0.2 \text{ g L}^{-1} \text{ NaHCO}_3$ , pH 5) was evaluated using a multiscale  
756 electrochemical approach. From the obtained results, the following conclusions can be  
757 summarized:

758 1. Horse chestnut extract was able to hinder to some extent the corrosion process of  
759 bronze, acting as a mixed-type inhibitor. The anticorrosive effectiveness of HCE was found to  
760 increase with its concentration up to an ‘optimum’ value of  $0.5 \text{ g L}^{-1}$ , and it improved with  
761 longer treatment times. The maximum inhibiting efficiencies reached ca. 85% and 94% in the  
762 presence of  $0.5 \text{ g L}^{-1}$  HCE, after 1-h and 14-h exposure, respectively. A further increase of the  
763 immersion time up to 36-h did not improve the protective properties of HCE. Although the

764 inhibition ability of HCE is not the highest desirable, the seeds of horse chestnut are readily  
765 available, in large scale and could be valorised as an inexpensive option for resource recovery.

766 2. EIS measurements showed that the inhibiting effect of HCE is mainly due to the  
767 formation of a thin protective film *via* the adsorption of its components on the bronze surface,  
768 which hindered to some extent the charge transfer process and stabilised the corrosion products,  
769 offering an improved protection.

770 3. Potentiodynamic polarisation measurements performed at different temperatures  
771 showed that the inhibition ability of HCE decreased slightly at higher temperatures. The  
772 thermodynamic parameters indicate that the adsorption mechanism of HCE on bronze surface is  
773 of physical nature.

774 4. SEM-EDS analysis indicated that the bronze dissolution process was mitigated in the  
775 presence of the inhibitor, and it produced a smoother bronze surface.

776 5. The reactivity of the bronze surface and the evolution of its susceptibility to undergo  
777 electron transfer reactions was investigated using the SECM in feedback operation, both in the  
778 absence and the presence of the inhibitor in the ‘optimized’ concentration. The analysis of the  
779 faradaic current measured at the tip allowed the rate constant for electron transfer between the  
780 metal surface and ferrocene-methanol as redox mediator to be determined. This process,  
781 dynamically and heterogeneously distributed throughout the substrate surface, allowed available  
782 active sites for electron transfer to be imaged in situ during their deactivation upon interaction  
783 with the components of the extract with corrosion inhibition characteristics.

784 6. A novel and promising method for SECM data evaluation on corrosion inhibitor  
785 adsorption is proposed. The distribution of the estimated values of the electron transfer rate  
786 constant from SECM maps was successfully fitted into Langmuir isotherm, by direct correlation  
787 with the surface coverage and blockage of the available sites for the electron donation. Results  
788 provided acceptable values for the rate and the equilibrium constants of the overall adsorption-  
789 desorption processes involving the substances present in the extract, supporting that a  
790 physisorption mechanism is the main responsible phenomena for the anticorrosive properties.

791 7. The microelectrochemical characterization of the inhibition characteristics of HCE for  
792 the corrosion protection of bronze correlated well with the data obtained using conventional  
793 electrochemical techniques. The applied methodology is regarded as particularly promising for

794 the investigation of the microscopically heterogeneous adsorption characteristics of green  
795 corrosion inhibitors on metals.

796 8. The inhibition effect of HCE might be related to one specific molecule or to a  
797 synergistic effect of the entire extract. Although, HPLC-PDA, GC-MS and FTIR analysis  
798 identified the most abundant compounds from HCE, but it was difficult to assign the inhibiting  
799 action to a particular constituent or group of constituents. Therefore, further studies are needed to  
800 completely understand the involved protection mechanism. This drawback is rather common  
801 when investigating corrosion inhibitors derived from plant extracts because they appear as  
802 complex mixtures of multiple constituents belonging to different functional groups.

803

#### 804 **Acknowledgements**

805 The authors thank Dr. Florin Popa from the Materials Science and Engineering  
806 Department, Technical University of Cluj-Napoca (Romania) for assistance in the SEM-EDS  
807 characterizations. The work was partially financed by the Spanish Ministry of Economy and  
808 Competitiveness (MINECO, Madrid) and the European Regional Development Fund, under  
809 grant CTQ2016-80522-P.

810 One of the authors (S. Varvara) gratefully acknowledge the support offered by Erasmus+  
811 Staff Mobility for Training Programme (2018).

812

#### 813 **Data availability**

814 The raw/processed data required to reproduce these findings cannot be shared at this time due to  
815 technical or time limitations.

816

#### 817 **References**

- 818 [1] Z. Wang, Y. Li, X. Jiang, C. Pan, Research Progress on Ancient Bronze Corrosion in  
819 Different Environments and Using Different Conservation Techniques: A Review, *MRS*  
820 *Adv.* 2 (2017) 2033–2041. doi:10.1557/adv.2017.222.
- 821 [2] F.J.R. de Oliveira, D.C.B. Lago, L.F. Senna, L.R.M. de Miranda, E. D’Elia, Study of  
822 patina formation on bronze specimens, *Mater. Chem. Phys.* 115 (2009) 761–770.  
823 doi:10.1016/j.matchemphys.2009.02.035.

- 824 [3] T. Kosec, H.O. Ćurković, A. Legat, Investigation of the corrosion protection of  
825 chemically and electrochemically formed patinas on recent bronze, *Electrochim. Acta.* 56  
826 (2010) 722–731. doi:10.1016/j.electacta.2010.09.093.
- 827 [4] G. Di Carlo, C. Giuliani, C. Riccucci, M. Pascucci, E. Messina, G. Fierro, M. Lavorgna,  
828 G.M. Ingo, Artificial patina formation onto copper-based alloys: Chloride and sulphate  
829 induced corrosion processes, *Appl. Surf. Sci.* 421 (2017) 120–127.  
830 doi:10.1016/j.apsusc.2017.01.080.
- 831 [5] B. Rosales, R. Vera, G. Moriena, Evaluation of the protective properties of natural and  
832 artificial patinas on copper. Part I. Patinas formed by immersion, *Corros. Sci.* 41 (1999)  
833 625–651. doi:10.1016/S0010-938X(98)00108-5.
- 834 [6] R.D.P.B. Hernández, I. V. Aoki, B. Tribollet, H.G. De Melo, Electrochemical impedance  
835 spectroscopy investigation of the electrochemical behaviour of copper coated with  
836 artificial patina layers and submitted to wet and dry cycles, *Electrochim. Acta.* 56 (2011)  
837 2801–2814. doi:10.1016/j.electacta.2010.12.059.
- 838 [7] W.A. Badawy, R.M. El-Sherif, H. Shehata, Electrochemical behavior of aluminum bronze  
839 in sulfate-chloride media, *J. Appl. Electrochem.* 37 (2007) 1099–1106.  
840 doi:10.1007/s10800-007-9362-9.
- 841 [8] C. Chiavari, E. Bernardi, C. Martini, F. Passarini, F. Ospitali, L. Robbiola, The  
842 atmospheric corrosion of quaternary bronzes: The action of stagnant rain water, *Corros.*  
843 *Sci.* 52 (2010) 3002–3010. doi:10.1016/j.corsci.2010.05.013.
- 844 [9] S. Aouadi, N. Souissi, Early stages of tin bronze corrosion in neutral aqueous chloride  
845 media: Electrochemical and FTIR investigations, *Mater. Corros.* 67 (2016) 1105–1113.  
846 doi:10.1002/maco.201608856.
- 847 [10] X. Liao, F. Cao, J. Zhang, Effect of sulphate on the corrosion behavior of bronze under a  
848 chloride-containing thin electrolyte layer, *Mater. Corros.* 69 (2018) 1412–1421.  
849 doi:10.1002/maco.201810132.
- 850 [11] L. Muresan, S. Varvara, E. Stupnišek-Lisac, H. Otmačić, K. Marušić, S. Horvat-  
851 Kurbegović, L. Robbiola, K. Rahmouni, H. Takenouti, Protection of bronze covered with  
852 patina by innocuous organic substances, *Electrochim. Acta.* 52 (2007) 7770–7779.  
853 doi:10.1016/j.electacta.2007.02.024.
- 854 [12] S. Varvara, R. Bostan, L. Gəinə, L.M. Muresan, Thiadiazole derivatives as inhibitors for

- 855 acidic media corrosion of artificially patinated bronze, *Mater. Corros.* 65 (2014) 1202–  
856 1214. doi:10.1002/maco.201307072.
- 857 [13] W. Qafsaoui, A.E. Taouil, M.W. Kendig, H. Cachet, S. Joiret, H. Perrot, H. Takenouti,  
858 Coupling of electrochemical, electrogravimetric and surface analysis techniques to study  
859 dithiocarbamate/bronze interactions in chloride media, *Corros. Sci.* 130 (2018) 190–202.  
860 doi:10.1016/j.corsci.2017.10.034.
- 861 [14] M.M. Antonijević, M.B. Petrović Mihajlović, Copper corrosion inhibitors. A review, *Int.*  
862 *J. Electrochem. Sci.* 3 (2008) 1–28. doi:10.1016/j.ijengsci.2004.12.001.
- 863 [15] M.M. Antonijević, M.B. Petrović Mihajlović, Copper Corrosion Inhibitors. Period 2008–  
864 2014. A Review, *Int. J. Electrochem. Sci.* 10 (2015) 1027–1053.  
865 doi:10.1016/j.ijengsci.2004.12.001.
- 866 [16] Ž.Z. Tasić, M.B. Petrović Mihajlović, M.B. Radovanović, M.M. Antonijević, New trends  
867 in corrosion protection of copper, *Chem. Pap.* 73 (2019) 2103–2132. doi:10.1007/s11696-  
868 019-00774-1.
- 869 [17] G. Laguzzi, L. Luvidi, Evaluation of the anticorrosive properties of benzotriazole alkyl  
870 derivatives on 6% Sn bronze alloy, *Surf. Coatings Technol.* 204 (2010) 2442–2446.  
871 doi:10.1016/j.surfcoat.2010.01.019.
- 872 [18] M. Finšgar, I. Milošev, Inhibition of copper corrosion by 1,2,3-benzotriazole: A review,  
873 *Corros. Sci.* 52 (2010) 2737–2749. doi:10.1016/j.corsci.2010.05.002.
- 874 [19] K. Marušić, H.O. Čurković, H. Takenouti, Inhibiting effect of 4-methyl-1-p-  
875 tolylimidazole to the corrosion of bronze patinated in sulphate medium, *Electrochim.*  
876 *Acta.* 56 (2011) 7491–7502. doi:10.1016/j.electacta.2011.06.107.
- 877 [20] I. Milošev, N. Kovačević, J. Kovač, A. Kokalj, The roles of mercapto, benzene and  
878 methyl groups in the corrosion inhibition of imidazoles on copper: I. Experimental  
879 characterization, *Corros. Sci.* 98 (2015) 107–118. doi:10.1016/j.corsci.2015.05.006.
- 880 [21] M.B. Petrović Mihajlović, M.B. Radovanović, Ž.Z. Tasić, M.M. Antonijević, Imidazole  
881 based compounds as copper corrosion inhibitors in seawater, *J. Mol. Liq.* 225 (2017) 127–  
882 136. doi:10.1016/j.molliq.2016.11.038.
- 883 [22] A. Dermaj, N. Hajjaji, S. Joiret, K. Rahmouni, A. Srhiri, H. Takenouti, V. Vivier,  
884 Electrochemical and spectroscopic evidences of corrosion inhibition of bronze by a  
885 triazole derivative, *Electrochim. Acta.* 52 (2007) 4654–4662.

- 886 doi:10.1016/j.electacta.2007.01.068.
- 887 [23] M.M. Antonijević, S.M. Milić, M.B. Petrović, Films formed on copper surface in chloride  
888 media in the presence of azoles, *Corros. Sci.* 51 (2009) 1228–1237.  
889 doi:10.1016/j.corsci.2009.03.026.
- 890 [24] S. Varvara, L.M. Muresan, K. Rahmouni, H. Takenouti, Evaluation of some non-toxic  
891 thiadiazole derivatives as bronze corrosion inhibitors in aqueous solution, *Corros. Sci.* 50  
892 (2008) 2596–2604. doi:10.1016/j.corsci.2008.06.046.
- 893 [25] D.C.B. Do Lago, L.F. De Senna, E.C.S. Soares, L.F. da Silva, D.S. Fernandes, A.S. Luna,  
894 E. D'Elia, The use of experimental design for the study of the corrosion of bronze  
895 pretreated with AMT in artificial rainwater, *Prog. Org. Coatings.* 76 (2013) 1289–1295.  
896 doi:10.1016/j.porgcoat.2013.03.032.
- 897 [26] H. Tian, W. Li, K. Cao, B. Hou, Potent inhibition of copper corrosion in neutral chloride  
898 media by novel non-toxic thiadiazole derivatives, *Corros. Sci.* 73 (2013) 281–291.  
899 doi:10.1016/j.corsci.2013.04.017.
- 900 [27] C. Monticelli, A. Balbo, J. Esvan, C. Chiavari, C. Martini, F. Zanotto, L. Marvelli, L.  
901 Robbiola, Evaluation of 2-(salicylideneimino) thiophenol and other Schiff bases as bronze  
902 corrosion inhibitors by electrochemical techniques and surface analysis, *Corros. Sci.* 148  
903 (2019) 144–158. doi:10.1016/j.corsci.2018.12.017.
- 904 [28] S. Varvara, M. Popa, L.M. Muresan, Corrosion inhibition of bronze by amino acids in  
905 aqueous acidic solutions, *Stud. Univ. Babeş-Bolyai Chem.* 3 (2009) 235–247.
- 906 [29] T. Wang, J. Wang, Y. Wu, The inhibition effect and mechanism of l-cysteine on the  
907 corrosion of bronze covered with a CuCl patina, *Corros. Sci.* 97 (2015) 89–99.  
908 doi:10.1016/j.corsci.2015.04.018.
- 909 [30] L.T. Popoola, Organic green corrosion inhibitors (OGCIs): A critical review, *Corros. Rev.*  
910 37 (2019) 71–102. doi:10.1515/corrrev-2018-0058.
- 911 [31] B.A. Abd-El-Nabey, A.H. Abdel-Gaber, M.E.S. Ali, E. Khamis, S. El-Housseiny,  
912 Inhibitive Action of cannabis plant extract on the corrosion of copper in 0.5 M H<sub>2</sub>SO<sub>4</sub>, *Int.*  
913 *J. Electrochem. Sci.* 8 (2013) 7124–7137.
- 914 [32] K. Krishnaveni, J. Ravichandran, Influence of aqueous extract of leaves of *Morinda*  
915 *tinctoria* on copper corrosion in HCl medium, *J. Electroanal. Chem.* 735 (2014) 24–31.  
916 doi:10.1016/j.jelechem.2014.09.032.

- 917 [33] M.A. Deyab, Egyptian licorice extract as a green corrosion inhibitor for copper in  
918 hydrochloric acid solution, *J. Ind. Eng. Chem.* 22 (2015) 384–389.  
919 doi:10.1016/j.jiec.2014.07.036.
- 920 [34] A.S. Fouda, M.A. Elmersi, B.S. Abou-Elmagd, Adsorption and inhibitive properties of  
921 methanol extract of *Euphorbia Heterophylla* for the corrosion of copper in 0.5 M nitric  
922 acid solutions, *Polish J. Chem. Technol.* 19 (2017) 95–103. doi:10.1515/pjct-2017-0014.
- 923 [35] F. Wedian, M.A. Al-Qudah, G.M. Al-Mazaideh, Corrosion inhibition of copper by  
924 *Capparis spinosa* L. extract in strong acidic medium: Experimental and density functional  
925 theory, *Int. J. Electrochem. Sci.* 12 (2017) 4664–4676. doi:10.20964/2017.06.47.
- 926 [36] A. Jmiai, B. El Ibrahimy, A. Tara, M. Chadili, S. El Issami, O. Jbara, A. Khallaayoun, L.  
927 Bazzi, Application of *Zizyphus Lotuse* - pulp of Jujube extract as green and promising  
928 corrosion inhibitor for copper in acidic medium, *J. Mol. Liq.* 268 (2018) 102–113.  
929 doi:10.1016/j.molliq.2018.06.091.
- 930 [37] H. Gerengi, K. Schaefer, H.I. Sahin, Corrosion-inhibiting effect of *Mimosa* extract on  
931 brass-MM55 corrosion in 0.5 M H<sub>2</sub>SO<sub>4</sub> acidic media, *J. Ind. Eng. Chem.* 18 (2012)  
932 2204–2210. doi:10.1016/j.jiec.2012.06.019.
- 933 [38] T. Ramde, S. Rossi, C. Zanella, Inhibition of the Cu<sub>65</sub>/Zn<sub>35</sub> brass corrosion by natural  
934 extract of *Camellia sinensis*, *Appl. Surf. Sci.* 307 (2014) 209–216.  
935 doi:10.1016/j.apsusc.2014.04.016.
- 936 [39] A.S. Fouda, K. Shalabi, A.A. Idress, *Ceratonia siliqua* extract as a green corrosion  
937 inhibitor for copper and brass in nitric acid solutions, *Green Chem. Lett. Rev.* 8 (2015)  
938 17–29. doi:10.1080/17518253.2015.1073797.
- 939 [40] H.S. Gadow, M.M. Motawea, H.M. Elabbasy, Investigation of myrrh extract as a new  
940 corrosion inhibitor for  $\alpha$ -brass in 3.5% NaCl solution polluted by 16 ppm sulfide, *RSC*  
941 *Adv.* 7 (2017) 29883–29898. doi:10.1039/c7ra04271j.
- 942 [41] B. Benzidia, H. Hammouch, A. Dermaj, H. Benassaoui, S. Abbout, N. Hajjaji,  
943 Investigation of green corrosion inhibitor based on aloe vera (*L.*) burm. F. for the  
944 protection of bronze B66 in 3% NaCl, *Anal. Bioanal. Electrochem.* 11 (2019) 165–177.
- 945 [42] R. Ben Channouf, N. Souissi, N. Bellakhal, *Juniperus communis* extract effect on bronze  
946 corrosion in natural 0.5 M chloride medium, *J. Mater. Sci. Chem. Eng.* 3 (2015) 21–29.  
947 doi:10.4236/msce.2015.311004.

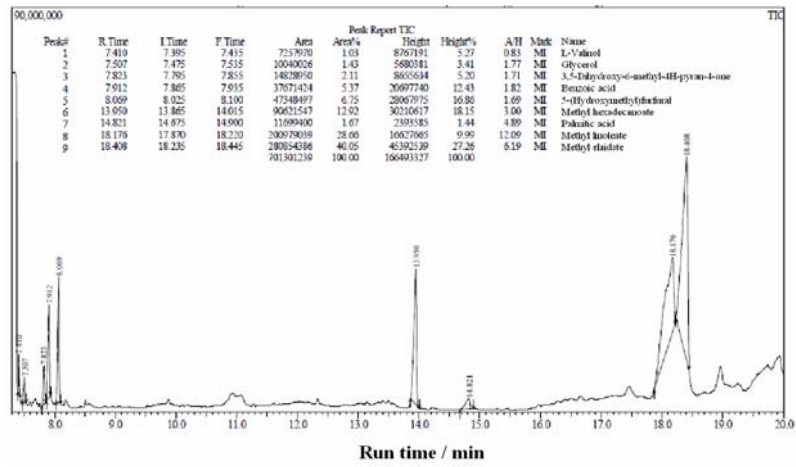
- 948 [43] A.K. Larios-Galvez, J. Porcayo-Calderon, V.M. Salinas-Bravo, J.G. Chacon-Nava, J.G.  
949 Gonzalez-Rodriguez, L. Martinez-Gomez, Use of *Salvia hispanica* as an eco-friendly  
950 corrosion inhibitor for bronze in acid rain, *Anti-Corrosion Methods Mater.* 64 (2017) 654–  
951 663. doi:10.1108/ACMM-02-2017-1760.
- 952 [44] S. Varvara, R. Bostan, O. Bobis, L. Găină, F. Popa, V. Mena, R.M. Souto, Propolis as a  
953 green corrosion inhibitor for bronze in weakly acidic solution, *Appl. Surf. Sci.* 426 (2017)  
954 1100–1112. doi:10.1016/j.apsusc.2017.07.230.
- 955 [45] V. Pourzarghan, H. Sarhaddi-Dadian, H. Bakhshandefard, Feasibility study of natural  
956 honey use as corrosion inhibitor in protecting the bronze artifacts, *Mediterr. Archaeol.*  
957 *Archaeom.* 17 (2017) 301–309. doi:10.5281/zenodo.1048935.
- 958 [46] G. Foca, A. Ulrici, M. Cocchi, C. Durante, M. Li Vigni, A. Marchetti, S. Sighinolfi, L.  
959 Tassi, Chapter 76 - Seeds of horse chestnut (*Aesculus Hippocastanum* L.) and their  
960 possible utilization for human consumption, in: V. Preedy, R. Watson, V. Patel (Eds.),  
961 *Nuts and Seeds in Health and Disease Prevention*, Academic Press, Cambridge, MA,  
962 2011, pp. 653-661, <https://doi.org/10.1016/B978-0-12-375688-6.10076-3>.
- 963 [47] L. Muresan, S. Varvara, G. Maurin, S. Dorneanu, Effect of some organic additives upon  
964 copper electrowinning from sulphate electrolytes, *Hydrometallurgy.* 54 (2000) 161–169.  
965 doi:10.1016/S0304-386X(99)00063-8.
- 966 [48] L. Muresan, L. Oniciu, M. Froment, G. Maurin, Inhibition of lead electrocrystallization by  
967 organic additives, *Electrochim. Acta.* 37 (1992) 2249–2254. doi:10.1016/0013-  
968 4686(92)85119-6.
- 969 [49] V.V. Parshutin, N.S. Sholtoyan, S.P. Sidel'nikova, A.V. Koval', I.I. Bulkhak, O.A.  
970 Bologa, V.N. Shofranskii, The influence of a water extract of horse chestnut fruit on the  
971 corrosion of St3 steel in water, *Surf. Eng. Appl. Electrochem.* 47 (2011) 276–283.  
972 doi:10.3103/S1068375511030161.
- 973 [50] R.F. Fan, D. Demaille, Preparation of tips for scanning electrochemical microscopy, in:  
974 A.J. Bard, M.V. Mirkin (Eds.), *Scanning Electrochem. Microscopy*, 2nd ed., CRC Press,  
975 Boca Raton, 2012, pp. 25-51.
- 976 [51] L. Guadagnini, C. Chiavari, C. Martini, E. Bernardi, L. Morselli, D. Tonelli, The use of  
977 scanning electrochemical microscopy for the characterisation of patinas on copper alloys,  
978 *Electrochim. Acta.* 56 (2011) 6598–6606. doi:10.1016/j.electacta.2011.04.080.



- 979 [52] V.L. Singleton, R. Orthofer, R.M. Lamuela-Raventos, Analysis of total phenols and other  
980 oxidation substrates and antioxidants by means of Folin–Ciocalteu reagent, *Methods*  
981 *Enzymol.* 299 (1999) 152–178.
- 982 [53] A. Arvouet–Grand, B. Vennat, A. Pourrat, P. Legret, Standardisation d'un extrait de  
983 propolis et identification des principaux constituants, *J. Pharm. Belg.* 4 (1994) 462–468
- 984 [54] I. Kapusta, B. Janda, B. Szajwaj, A. Stochmal, S. Piacente, C. Pizza, F. Franceschi, C.  
985 Franz, W. Oleszek, Flavonoids in horse chestnut (*Aesculus hippocastanum*) seeds and  
986 powdered waste water byproducts, *J Agric. Food Chem.* 55(2007) 8485-8490.  
987 doi:10.1021/jf071709t.
- 988 [55] V.A.Kurkin, P.V. Belov, V.M. Ryzhov, Quantitative determination of total flavonoids in  
989 horse chestnut *Aesculus hippocastanum* buds, *Pharm. Chem. J.* 53(2019) 155-159.  
990 doi:10.1007/s11094-019-01970-9
- 991 [56] F. Bentiss, M. Lebrini, M. Lagrenée, Thermodynamic characterization of metal  
992 dissolution and inhibitor adsorption processes in mild steel/2,5-bis(n-thienyl)-1,3,4-  
993 thiadiazoles/ hydrochloric acid system, *Corros. Sci.* 47 (2005) 2915–2931.  
994 doi:10.1016/j.corosci.2005.05.034.
- 995 [57] A. Popova, M. Christov, A. Vasilev, Mono- and dicationic benzothiazolic quaternary  
996 ammonium bromides as mild steel corrosion inhibitors: Part III: Influence of the  
997 temperature on the inhibition process, *Corros. Sci.* 94 (2015) 70–78.  
998 doi:10.1016/j.corosci.2015.01.039.
- 999 [58] I.D. Raistrick, J.R. MacDonald, D.R. Franceschetti, The electrical analogs of physical and  
1000 chemical processes, in: J.R. MacDonald (Ed.), *Impedance Spectrosc. Emphasizing Solid*  
1001 *Mater. Syst.*, John Wiley & Sons, New York, NY, 1987: pp. 27–84.
- 1002 [59] K. Rahmouni, N. Hajjaji, M. Keddami, A. Srhiri, H. Takenouti, The inhibiting effect of 3-  
1003 methyl 1,2,4-triazole 5-thione on corrosion of copper in 3% NaCl in presence of sulphide,  
1004 *Electrochim. Acta.* 52 (2007) 7519–7528. doi:10.1016/j.electacta.2006.12.079.
- 1005 [60] G.J. Brug, A.L.G. van der Eeden, M. Sluyters-Rehbach, J.H. Sluyters, The analysis of  
1006 electrode impedances complicated by the presence of a constant phase element, *J.*  
1007 *Electroanal. Chem.* 176 (1984) 275–295. doi:10.1016/S0022-0728(84)80324-1.
- 1008 [61] I. Epelboin, C. Gabrielli, M. Keddami, H. Takenouti, A-C impedance measurements  
1009 applied to corrosion studies and corrosion rate determination, in: F. Mansfeld, U. Bertocci

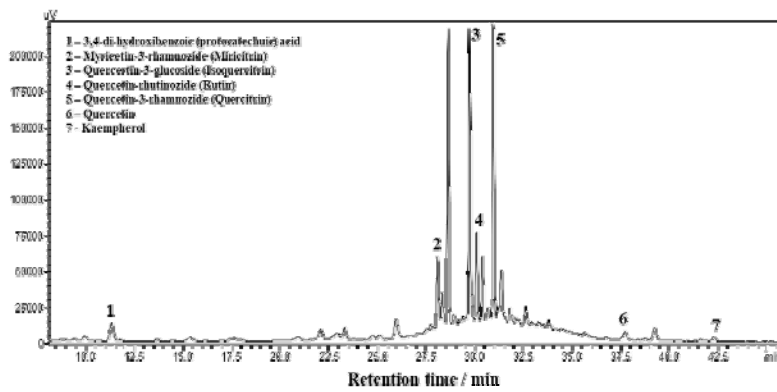
- 1010 (Eds.), *Electrochem. Corros. Testing*, STP 727, American Society for Testing and  
1011 Materials, Philadelphia, PA, 1981: pp. 150–192.
- 1012 [62] E.E. Oguzie, Evaluation of the inhibitive effect of some plant extracts on the acid  
1013 corrosion of mild steel, *Corros. Sci.* 50(2008) 2993-2998. doi:10.1016/j.corsci.08.08.004
- 1014 [63] C. Lefrou, R. Cornut, Analytical expressions for quantitative scanning electrochemical  
1015 microscopy (SECM), *ChemPhysChem.* 11 (2010) 547–556. doi:10.1002/cphc.200900600.
- 1016 [64] Y. Yu, Y. Gao, K. Hu, P.Y. Blanchard, J.M. Noël, T. Nareshkumar, K.L. Phani, G.  
1017 Friedman, Y. Gogotsi, M. V. Mirkin, Electrochemistry and electrocatalysis at single gold  
1018 nanoparticles attached to carbon nanoelectrodes, *ChemElectroChem.* 2 (2015) 58–63.  
1019 doi:10.1002/celec.201402312.
- 1020 [65] S. Marzorati, L. Verotta, S.P. Trasatti, Green corrosion inhibitors from natural sources and  
1021 biomass wastes, *Molecules* 24 (2019) 48–71. doi:10.3390/molecules24010048.
- 1022 [66] R. Cornut, C. Lefrou, New analytical approximation of feedback approach curves with a  
1023 microdisk SECM tip and irreversible kinetic reaction at the substrate, *J. Electroanal.*  
1024 *Chem.* 621 (2008) 178–184. doi:10.1016/j.jelechem.2007.09.021.
- 1025 [67] C. Cannes, F. Kanoufi, A.J. Bard, Cyclic voltammetry and scanning electrochemical  
1026 microscopy of ferrocenemethanol at monolayer and bilayer-modified gold electrodes, *J.*  
1027 *Electroanal. Chem.* 547 (2003) 83–91. doi:10.1016/S0022-0728(03)00192-X.
- 1028 [68] D.S. Karpovich, G.J. Blanchard, Direct measurement of the adsorption kinetics of  
1029 alkanethiolate self-assembled monolayers on a microcrystalline gold surface, *Langmuir.*  
1030 10 (1994) 3315–3322. doi:10.1021/la00021a066.
- 1031 [69] J.A. Ramírez-Cano, L. Veleva, Direct measurement of the adsorption kinetics of 2-  
1032 mercaptobenzothiazole on a microcrystalline copper surface, *Rev. Metal.* 52 (2016) e064.  
1033 doi:10.3989/revmetalm.064.
- 1034 [70] J.A. Ramírez-Cano, L. Veleva, R.M. Souto, B.M. Fernández-Pérez, Investigating metal-  
1035 inhibitor interaction with EQCM and SVET: 3-amino-1,2,4-triazole on Au, Cu and Au–Cu  
1036 galvanic coupling, *Mater. Corros.* 69 (2018) 115–124. doi:10.1002/maco.201709564.
- 1037 [71] A.Y. Musa, A.A. Khadom, A.A.H. Kadhum, M.S. Takriff, A.B. Mohamad, The role of 4-  
1038 amino-5-phenyl-4H-1,2,4-triazole-3-thiol in the inhibition of nickel-aluminum bronze  
1039 alloy corrosion: Electrochemical and DFT studies, *Res. Chem. Intermed.* 38 (2012) 91–  
1040 103. doi:10.1007/s11164-011-0328-5.

- 1041 [72] J.C. D'Ars De Figueiredo, V.F.C. De Lins, V.M. De Bellis, Inhibiting effect of  
1042 dithiocarbamate on TM 23 bronze alloy corrosion in acid medium, *Corros. Eng. Sci.*  
1043 *Technol.* 48 (2013) 288–293. doi:10.1179/1743278212Y.0000000075.
- 1044 [73] D.E. Millan-Ocampo, J.A. Hernandez-Perez, J. Porcayo-Calderon, J.P.F. De los Ríos, L.L.  
1045 Landeros-Martínez, V.M. Salinas-Bravo, J.G. Gonzalez-Rodriguez, L. Martinez,  
1046 Experimental and theoretical study of Ketoconazole as corrosion inhibitor for bronze in  
1047 NaCl+Na<sub>2</sub>SO<sub>4</sub>solution, *Int. J. Electrochem. Sci.* 12 (2017) 11428–11445.  
1048 doi:10.20964/2017.12.22.



A

1049

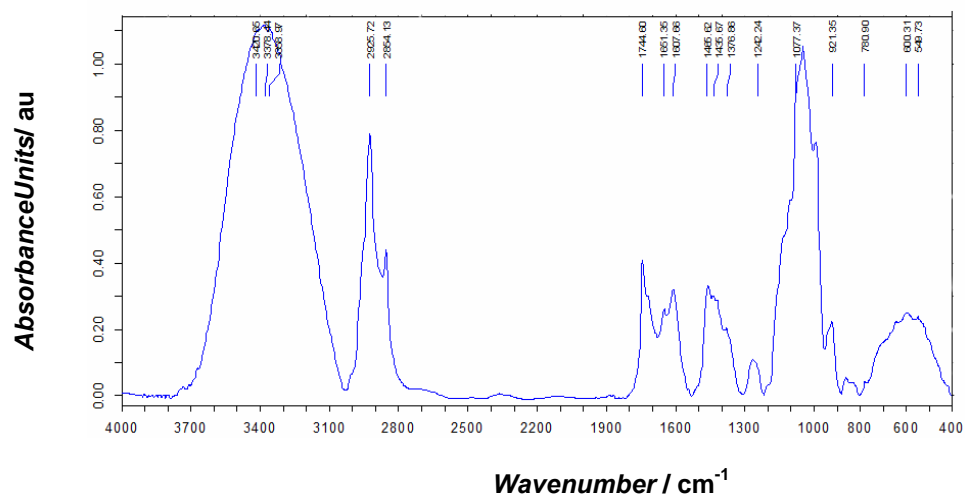


B

1050

1051 **Figure 1.** Characterization of the ethanolic extract of horse chestnut fruit by: (A) GC-MS and  
 1052 (B) HPLC-PDA chromatography.

1053



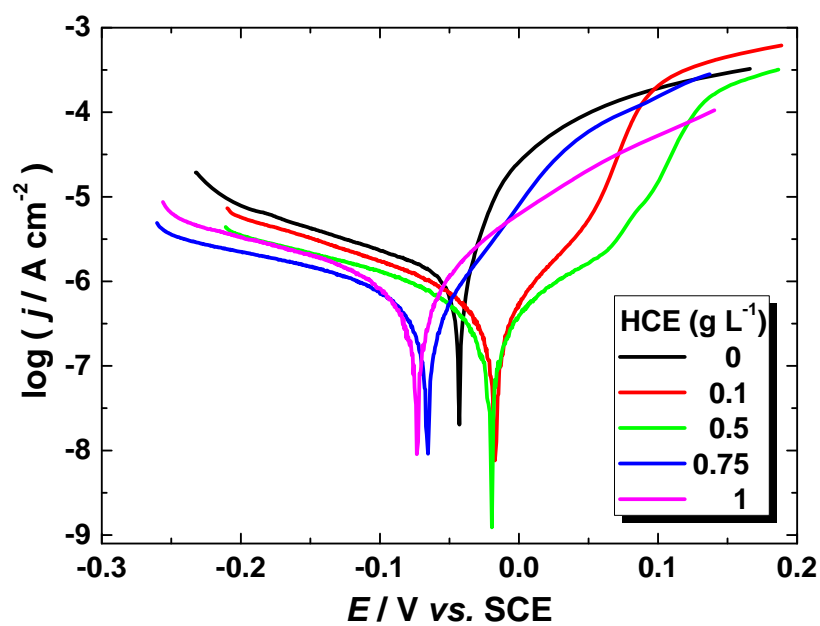
1054

1055

1056

1057

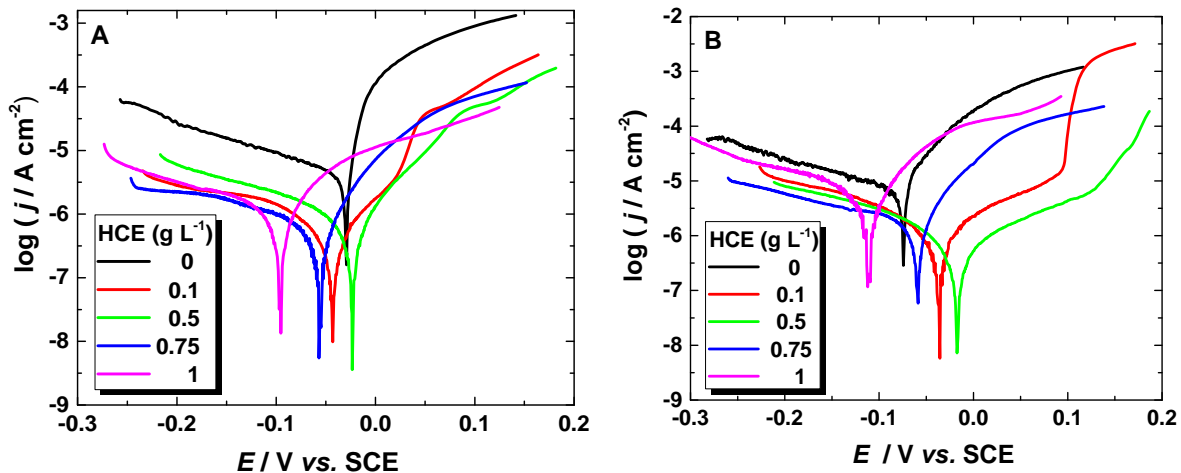
**Figure 2.** FTIR absorption spectrum of the horse chestnut extract.



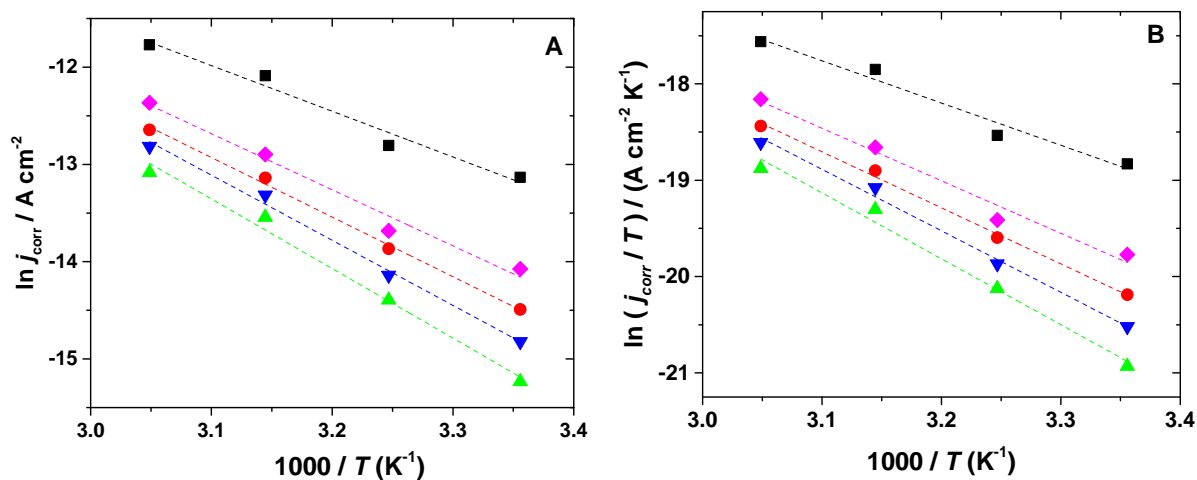
1058

**Figure 3.** Potentiodynamic polarization curves recorded for bronze samples immersed in  $0.2 \text{ g L}^{-1} \text{ Na}_2\text{SO}_4 + 0.2 \text{ g L}^{-1} \text{ NaHCO}_3 + x \text{ g L}^{-1} \text{ HCE}$  (pH 5) solution at 298 K.

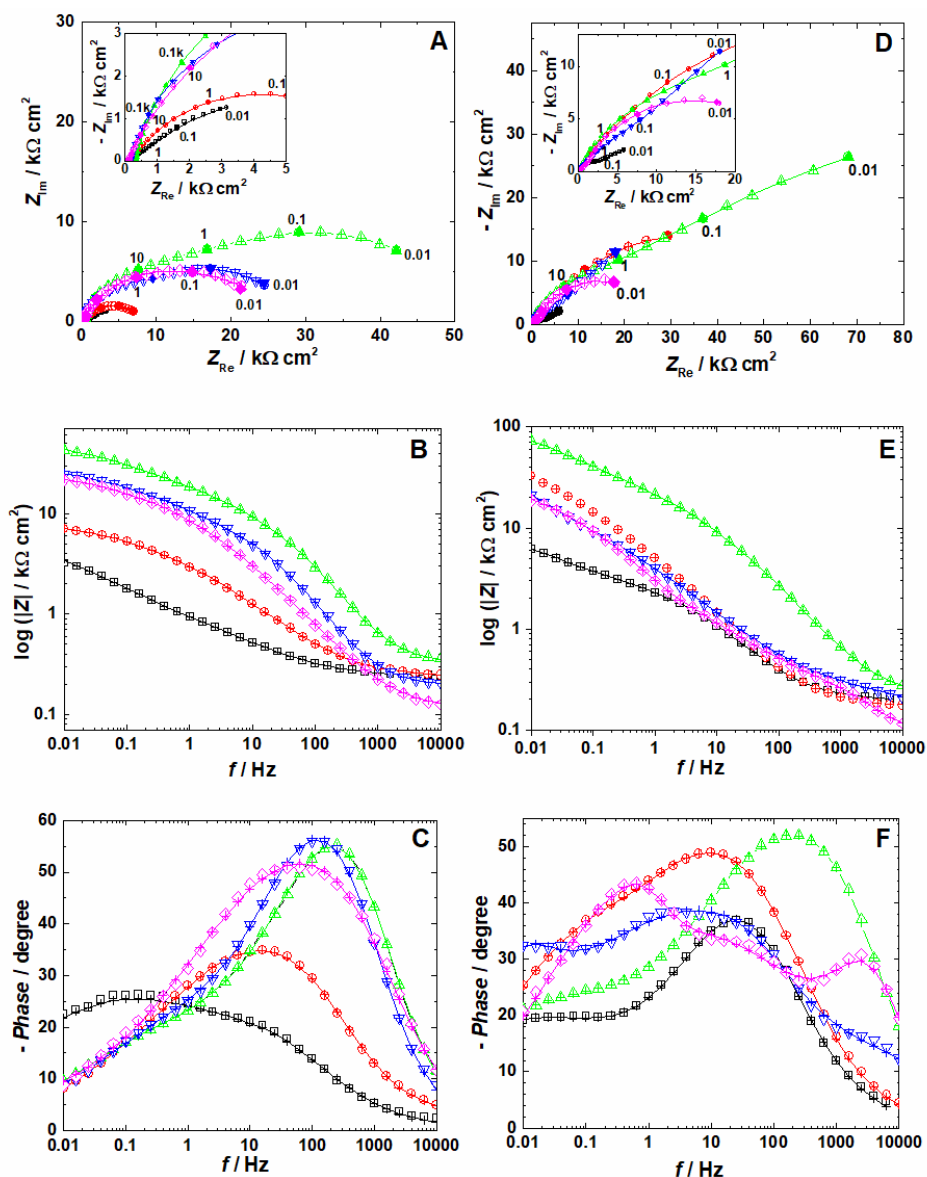
1061



1062  
 1063 **Figure 4.** Potentiodynamic polarization curves recorded for bronze electrodes immersed in 0.2 g  
 1064 L<sup>-1</sup> Na<sub>2</sub>SO<sub>4</sub> + 0.2 g L<sup>-1</sup> NaHCO<sub>3</sub> + x g L<sup>-1</sup> HCE (pH 5) solution at various temperatures: (A) 308  
 1065 K and (B) 328 K.  
 1066  
 1067



1068  
 1069 **Figure 5.** Arrhenius plots of  $\ln(j_{\text{corr}})$  vs.  $1/T$  (A) and of  $\ln(j_{\text{corr}}/T)$  vs.  $1/T$  (B) for bronze samples  
 1070 immersed in 0.2 g L<sup>-1</sup> Na<sub>2</sub>SO<sub>4</sub> + 0.2 g L<sup>-1</sup> NaHCO<sub>3</sub> (pH 5) solution without and with the addition  
 1071 of HCE. HCE concentration: (■) 0, (●) 0.1, (▲) 0.5, (▼) 0.75, and (◆) 1 g L<sup>-1</sup>.  
 1072



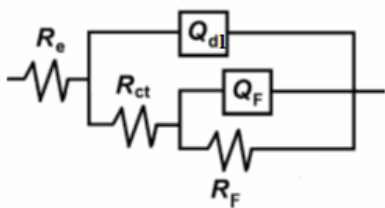
1073

1074 **Figure 6.** Nyquist plots (A,D) and Bode plots (B,C,E,F) recorded for bronze samples solutions  
 1075 after 1 h (A-C) and 14 h (D-F) immersion in  $0.2 \text{ g L}^{-1} \text{ Na}_2\text{SO}_4 + 0.2 \text{ g L}^{-1} \text{ NaHCO}_3 + x \text{ g L}^{-1}$   
 1076 HCE (pH 5) solution. HCE concentrations: ( $\square$ ) 0, ( $\circ$ ) 0.1, ( $\Delta$ ) 0.5, ( $\nabla$ ) 0.75 and ( $\diamond$ )  $1 \text{ g L}^{-1}$ .

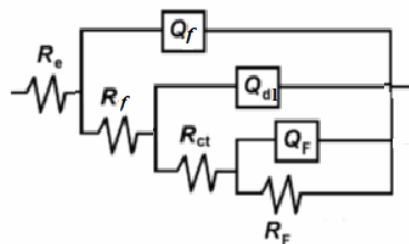
1077 Symbols correspond to measured data, and solid lines to the simulated results using the  
 1078 equivalent circuits depicted in Figure 7. The numbers in Nyquist diagrams refer to frequency in  
 1079 Hz.

1080

1081



A



B

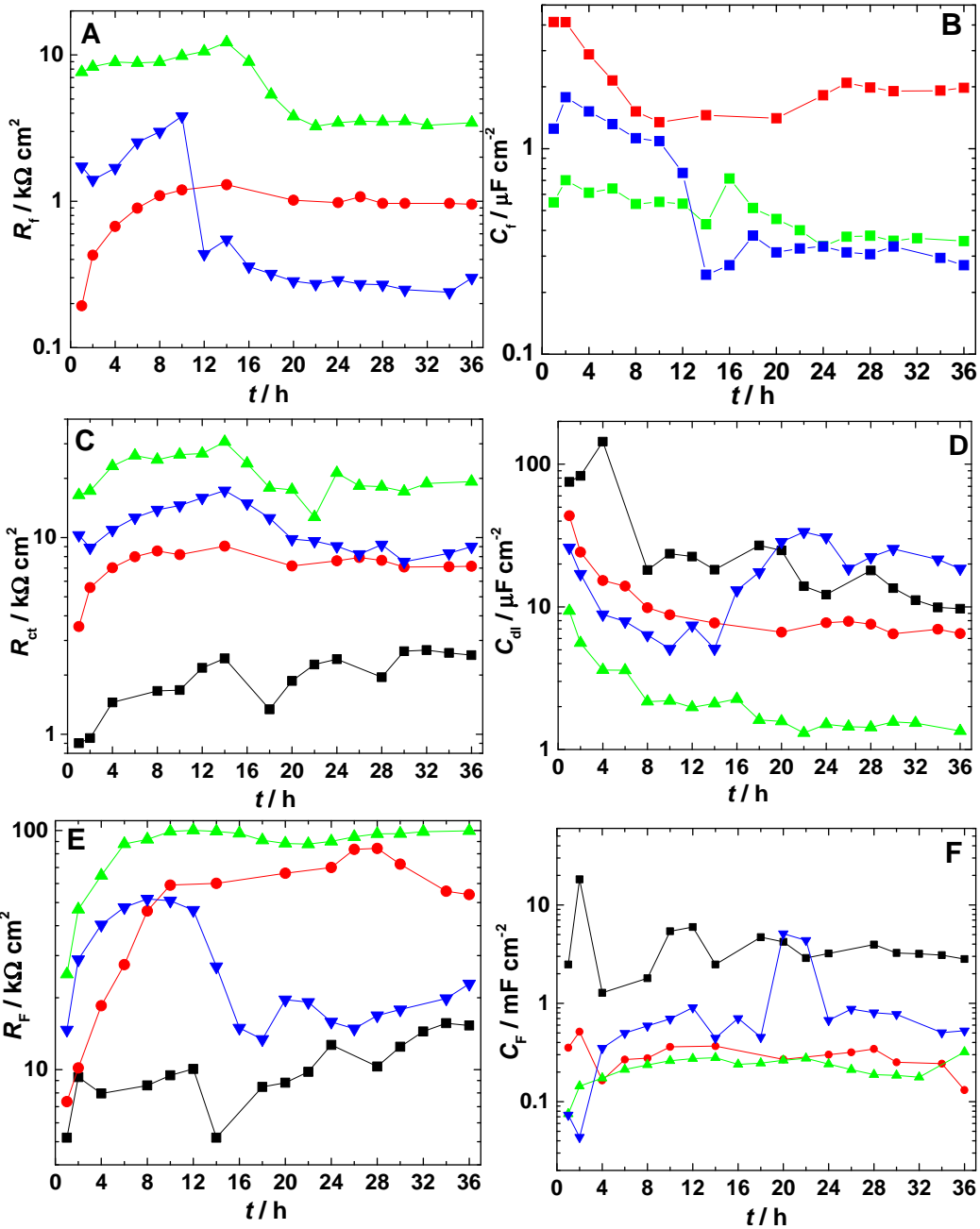
1082

1083

1084 **Figure 7.** Equivalent electrical circuits used to fit the experimental impedance spectra  
 1085 containing: (A) 2 and (B) 3 time constants.



1086



1087

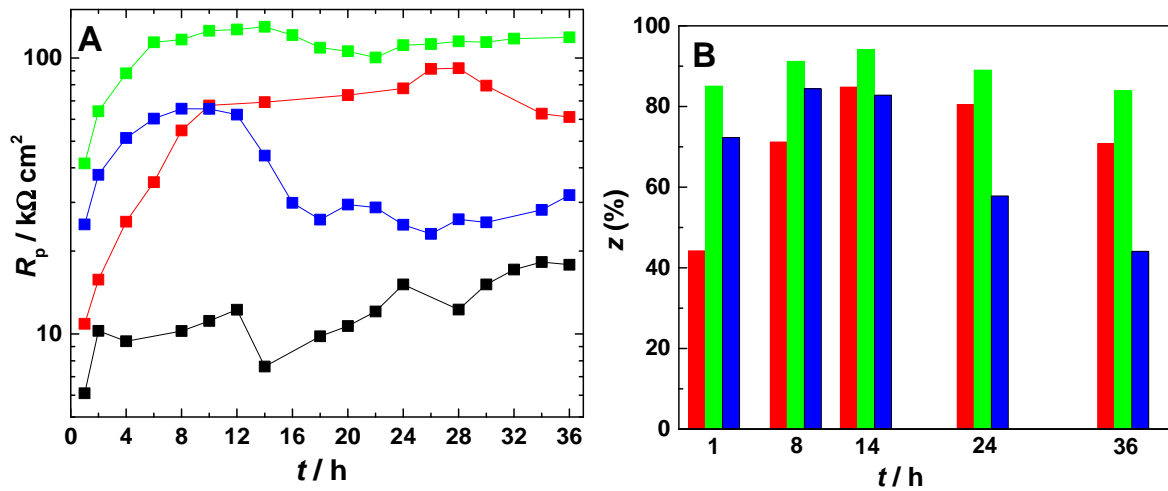
1088

1089

1090 **Figure 8.** Time evolution of the electrochemical impedance parameters of bronze corrosion  
 1091 during immersion in 0.2 g L<sup>-1</sup> Na<sub>2</sub>SO<sub>4</sub> + 0.2 g L<sup>-1</sup> NaHCO<sub>3</sub> + x g L<sup>-1</sup> HCE (pH 5) solution. HCE  
 1092 concentrations: (■) 0, (●) 0.1, (▲) 0.5, and (▼) 0.75 g L<sup>-1</sup>.

1093

1094

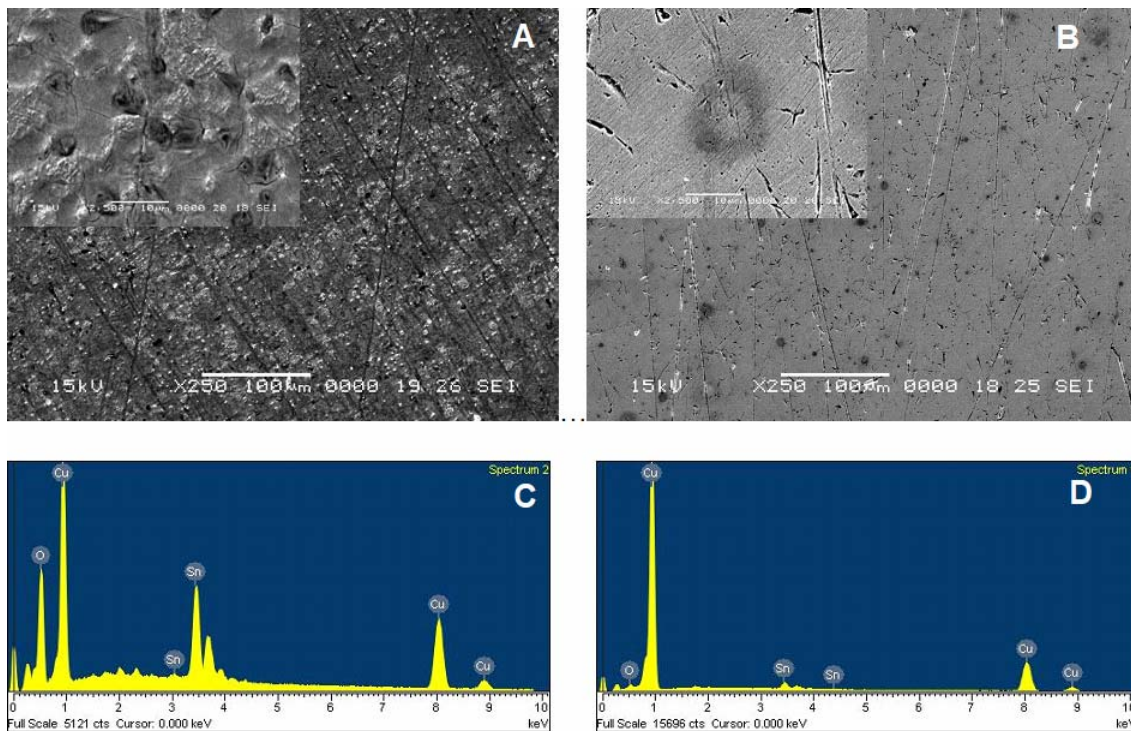


1095

1096 **Figure 9.** Time evolution of (A) the polarisation resistance and (B) the inhibition efficiency for  
 1097 bronze samples during immersion in 0.2 g L<sup>-1</sup> Na<sub>2</sub>SO<sub>4</sub> + 0.2 g L<sup>-1</sup> NaHCO<sub>3</sub> + x g L<sup>-1</sup> HCE (pH 5)  
 1098 solution. HCE concentrations: (■) 0, (■) 0.1, (■) 0.5, and (■) 0.75 g L<sup>-1</sup>.

1099

1100

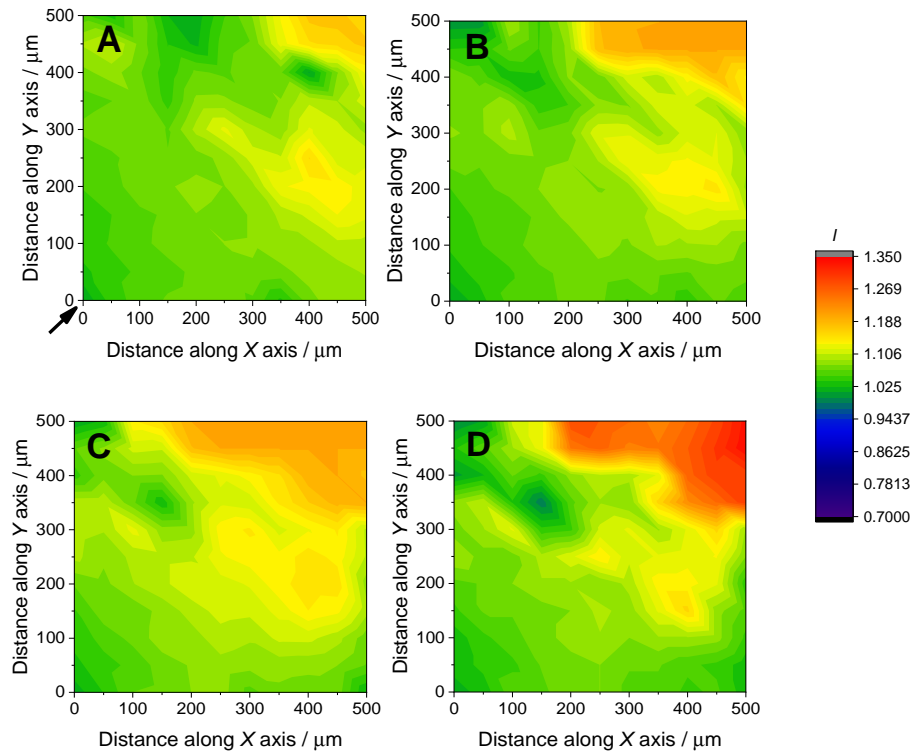


1101

1102 **Figure 10.** (A,B) SEM micrographs and (C,D) EDS analysis of bronze samples retrieved from  
 1103 0.2 g L<sup>-1</sup> Na<sub>2</sub>SO<sub>4</sub> + 0.2 g L<sup>-1</sup> NaHCO<sub>3</sub> (pH 5) solution after 36 h exposure: (A,C) in the absence,  
 1104 and (B,D) in the presence of 0.5 g L<sup>-1</sup> HCE.  
 1105

1105

1106



1107

1108

1109

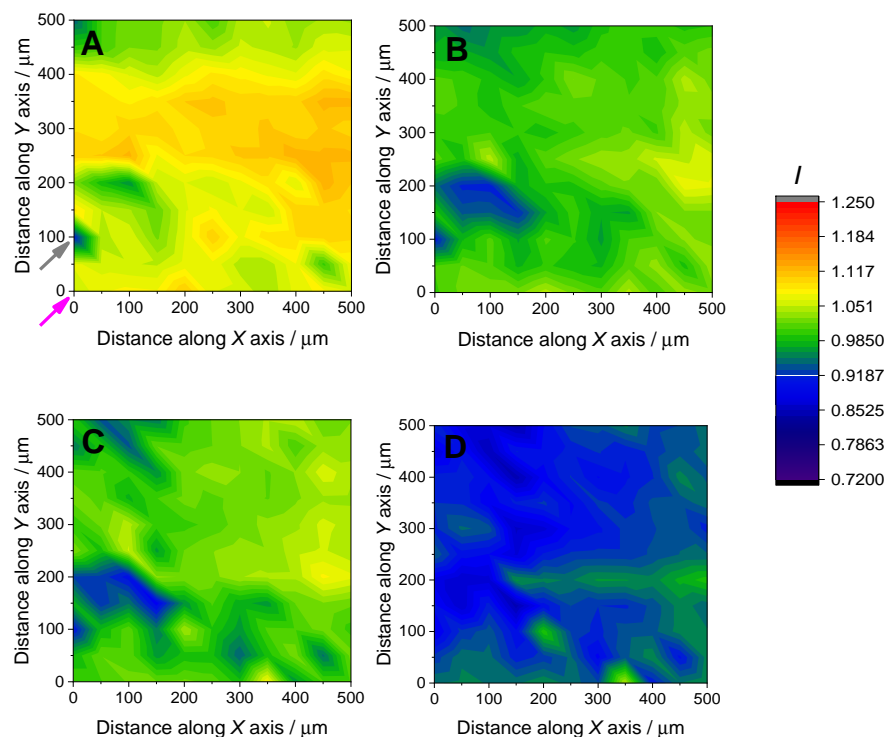
1110

1111

1112

1113

**Figure 11.** SECM maps of a bronze surface imaged in  $0.2 \text{ g L}^{-1} \text{ Na}_2\text{SO}_4 + 0.2 \text{ g L}^{-1} \text{ NaHCO}_3$  (pH 5) solution after: (A) 23, (B) 50, (C) 70, and (D) 140 min immersion. Tip-to-substrate distance:  $15 \text{ }\mu\text{m}$ . Tip potential:  $+0.50 \text{ V vs. Ag/AgCl/KCl(sat.)}$ . The sample was left unbiased at its spontaneous OCP. The arrow in (A) indicates the location selected for recording the Z-approach curves shown in Figure 13A.

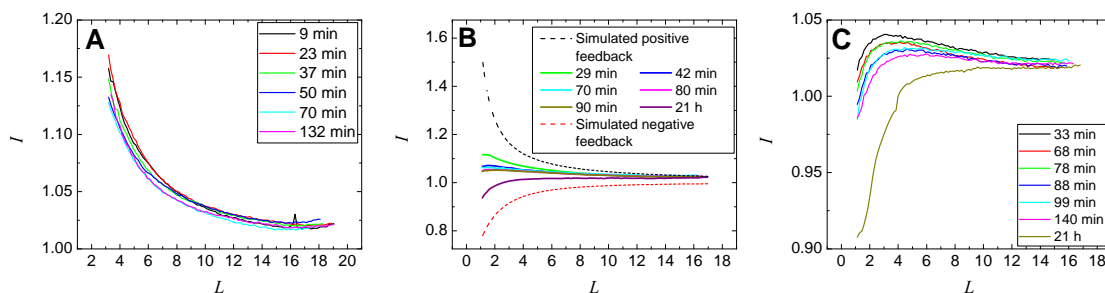


1114

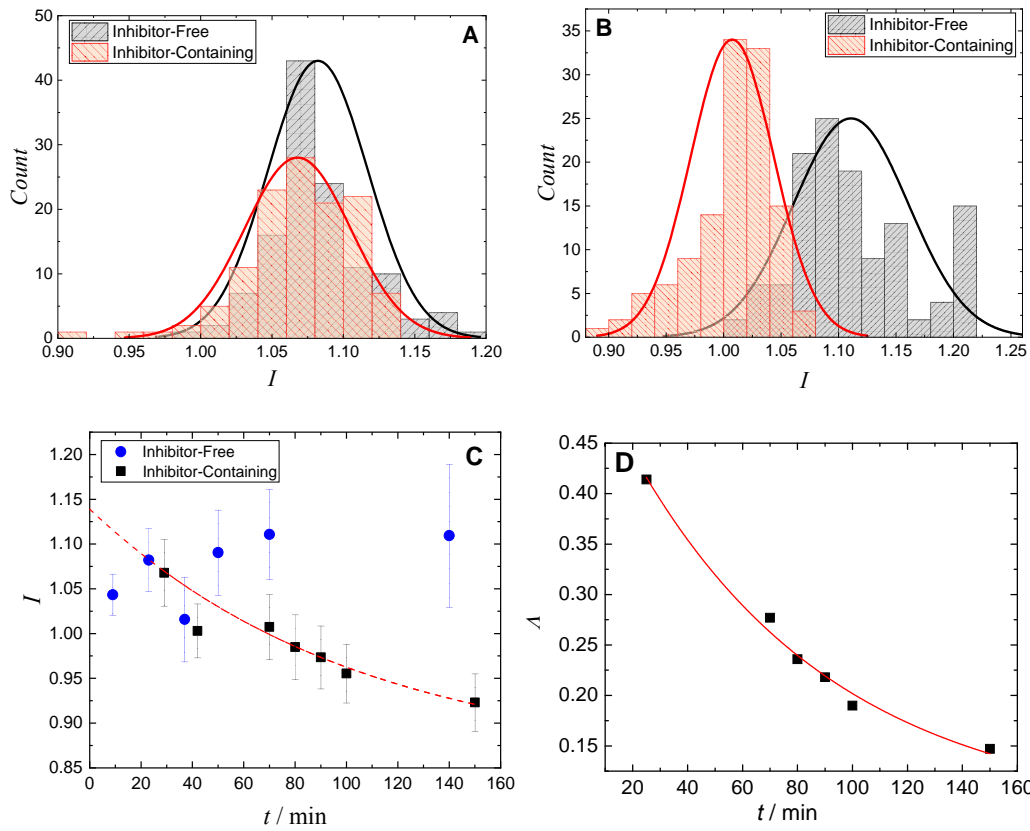
1115

1116 **Figure 12.** SECM maps of a bronze surface imaged in  $0.2 \text{ g L}^{-1} \text{ Na}_2\text{SO}_4 + 0.2 \text{ g L}^{-1} \text{ NaHCO}_3 +$   
 1117  $0.2 \text{ g L}^{-1} \text{ HCE}$  (pH 5) solution after: (A) 29, (B) 42, (C) 70, and (D) 150 min immersion. Tip-to-  
 1118 substrate distance:  $15 \text{ } \mu\text{m}$ . Tip potential:  $+0.50 \text{ V vs. Ag/AgCl/KCl(sat.)}$ . The sample was left  
 1119 unbiased at its spontaneous OCP. The arrows in (A) indicate the locations selected for recording  
 1120 the Z-approach curves shown in Figure 13B (purple) and Figure 13C (grey).

1121



1122  
 1123 **Figure 13.** Normalized SECM Z-approach curves measured over bronze surfaces immersed in  
 1124  $0.2 \text{ g L}^{-1} \text{ Na}_2\text{SO}_4 + 0.2 \text{ g L}^{-1} \text{ NaHCO}_3 + x \text{ g L}^{-1} \text{ HCE}$  (pH 5) solution. HCE concentrations: (A) 0,  
 1125 and (B,C)  $0.5 \text{ g L}^{-1}$ . The actual locations at the surface of the bronze samples are indicated with  
 1126 arrows in: (A) black arrow in Figure 11A, (B) purple arrow in Figure 12A, and (C) grey arrow in  
 1127 Figure 12A. Tip potential:  $+0.50 \text{ V vs. Ag/AgCl/KCl(sat.)}$ . Scan rate:  $1 \mu\text{m s}^{-1}$ . Legend indicates  
 1128 the immersion time elapsed in test solution. The X axis gives the normalized distance  $L = d/a$ ,  
 1129 where  $d$  is the absolute distance along the Z axis, and  $a$  is the radius of the Pt microelectrode.  
 1130

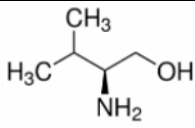
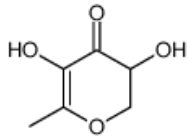
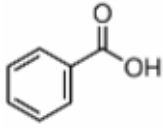
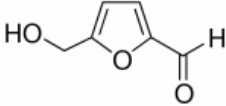
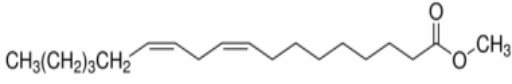
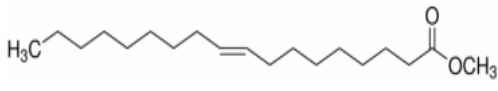


1131

1132

1133 **Figure 14.** (A,B) Typical histograms derived from the SECM scans recorded for bronze samples  
 1134 immersed in  $0.2 \text{ g L}^{-1} \text{ Na}_2\text{SO}_4 + 0.2 \text{ g L}^{-1} \text{ NaHCO}_3 + x \text{ g L}^{-1} \text{ HCE}$  (pH 5,  $x = 0; 0.5$ ) solution for:  
 1135 (A) 23-29 and (B) 70 min. (C) Time evolution of the (C) average limiting current value from the  
 1136 Gaussian distributions in the histograms and (D) resulting adimensional kinetic constant. Error  
 1137 bars in (C) account for the standard deviations  $\sigma$  of the Gaussian fits.

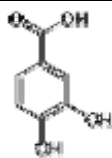
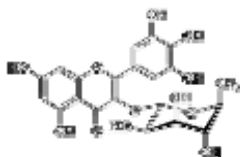
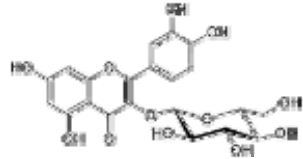
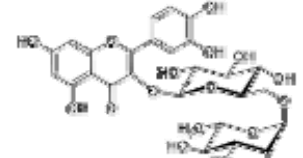
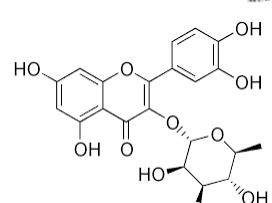
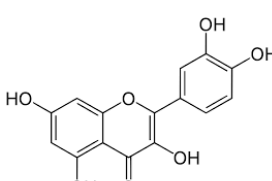
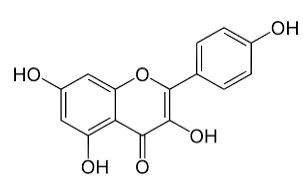
1138 **Table 1.** Molecular structures of the main components of HCE identified using GC-MS, and relative peak  
 1139 area in the GC-MS spectrum.

Identified compound	Molecular structure	Relative peak area (%)
L-Valinol		1.07
3,5-Dihydroxy-6-methyl-2,3-dihydro-(4H)-pyran-4-one		2.11
Benzoic acid		5.37
5-(Hydroxymethyl)furfural		6.75
Methyl hexadecanoate	$\text{CH}_3(\text{CH}_2)_{13}\text{CH}_2\text{COOCH}_3$	12.9
Palmitic acid	$\text{CH}_3(\text{CH}_2)_{13}\text{CH}_2\text{COOH}$	1.67
Methyl linoleate		28.7
Methyl elaidate		40.1

1140

1141

1142 **Table 2.** Molecular structure and concentration of the main phenolic acid and flavonoid compounds  
 1143 identified in horse chestnut (*Aesculus hippocastanum*) extract by HPLC- PDA.

No.	Identified Compound	Retention time (min)	Concentration (ppm)	Similarity with standard	Molecular structure
1	Protocatechuic acid (3,4-dihydroxybenzoic acid)	11.3	10.03	0.996	
2	Myricitrin (Myricetin-3-rhamnozide)	28.6	45.39	0.998	
3	Isoquercitrin (Quercetin-3-glucozide)	29.7	114.99	0.996	
4	Rutin (Quercetin rhamnizide)	30.07	43.79	0.997	
5	Quercitrin (Quercetin-3-rhamnozide)	30.9	89.69	0.995	
6	Quercetin	37.7	2.18	0.999	
7	Kaempferol	42.2	1.81	0.998	

1144



1145 **Table 3.** Corrosion parameters for bronze immersed in 0.2 g L<sup>-1</sup> Na<sub>2</sub>SO<sub>4</sub> + 0.2 g L<sup>-1</sup> NaHCO<sub>3</sub> + *x* g L<sup>-1</sup>  
 1146 HCE (pH 5) solution at 298 K.

$C_{\text{HCE}}/\text{g L}^{-1}$	$E_{\text{corr}}/\text{V vs. SCE}$	$j_{\text{corr}}/\mu\text{A cm}^{-2}$	$ \beta_{\text{c}} /\text{mV dec}^{-1}$	$\beta_{\text{a}}/\text{mV dec}^{-1}$	$Z(\%)$
0	-42.9	2.00	186.8	34.4	-
0.1	-16.5	0.51	186.2	64.1	74.5
0.5	-19.9	0.25	175.3	95.4	87.5
0.75	-65.2	0.37	186.2	54.5	81.7
1	-76.2	0.77	200.7	84.5	61.5

1147

1148 **Table 4.** Corrosion parameters for bronze immersed in 0.2 g L<sup>-1</sup> Na<sub>2</sub>SO<sub>4</sub> + 0.2 g L<sup>-1</sup> NaHCO<sub>3</sub> + *x* g L<sup>-1</sup>  
 1149 HCE (pH 5) solution at various temperatures.

$C_{\text{HCE}} / \text{g L}^{-1}$	$T / \text{K}$	$E_{\text{corr}} / \text{V vs. SCE}$	$j_{\text{corr}} / \mu\text{A cm}^{-2}$	$ \beta_{\text{c}}  / \text{mV dec}^{-1}$	$\beta_{\text{a}} / \text{mV dec}^{-1}$	$z$ (%)	$E_{\text{a}} / \text{kJ mol}^{-1}$	$\Delta H_{\text{a}} / \text{kJ mol}^{-1}$	$\Delta S_{\text{a}} / \text{J mol}^{-1}$
0	308	-29.46	2.75	214.1	16.2	-			
	318	-42.23	5.63	338.3	18.8	-	38.9	36.4	-233.4
	328	-80.24	7.74	252.3	48.3	-			
0.1	308	-43.18	0.95	225.5	107.9	65.4			
	318	-59.80	2.07	178.5	146.4	63.2	50.9	48.3	-204.3
	328	-37.05	3.22	303.8	230.4	58.3			
0.5	308	-44.75	0.56	179.3	126.5	79.6			
	318	-37.17	1.31	226.7	98.2	76.6	59.5	56.8	-181.5
	328	-17.60	2.08	152.6	168.4	73.1			
0.75	308	-55.86	0.72	252.6	53.6	73.7			
	318	-50.57	1.65	317.3	54.6	70.7	55.7	53.0	-191.3
	328	-59.12	2.72	302.5	56.6	64.9			
1	308	-96.15	1.14	221.2	68.6	58.4			
	318	-102.37	2.51	149.5	49.6	55.5	47.9	45.3	211.7
	328	-110.75	4.26	135.6	63.2	44.9			

1150 **Table 5.** Time evolution of the estimated kinetic constant rates for the electron transfer reaction of a  
1151 bronze sample immersed in 0.2 g L<sup>-1</sup> Na<sub>2</sub>SO<sub>4</sub> + 0.2 g L<sup>-1</sup> NaHCO<sub>3</sub> + 0.5 g L<sup>-1</sup> HCE (pH 5). They were  
1152 determined from the Z-approach curves shown in Figure 12B.

<i>t</i>	29 min	42 min	70 min	80 min	90 min	21 h
$k \times 10^3 / \text{s}^{-1}$	7.3	5.2	4.9	4.5	4.4	2.1

1153

1154

1155

1156

1157

1158